

ABSTRACT

LO, WILLIAM CHUNG HEI. Characterization of Hydrated Tungsten Oxides for Electrochemical Energy Storage. (Under the direction of Dr. Veronica Augustyn)

As global energy demands increase, so does the demand for electrochemical energy storage. The search for a sustainable energy source continues along with the search for a high energy density, high power energy storage medium, which are essential because sustainable energy sources such as solar energy provide peak energy output only at certain times of the day. Electrochemical energy storage devices are good candidates for storage, since they are generally highly efficient, can store large amounts of energy, and can have fast response times. Current technologies can provide either high energy density (batteries) or high power density (capacitors). Nanostructured materials can exhibit both high power and high energy density due to their high surface areas, but have drawbacks for large scale applications that require large amounts of materials and high volumetric energy densities. Effectively combining both high energy and high power in bulk, redox-active materials has not been demonstrated.

The motivation for this research is that the presence of structural water in bulk layered materials may enhance the power density of electrochemical energy storage devices. Structural water can lead to rapid proton transport via the Grotthus mechanism, whereby protons move along the structural water molecules via the hydrogen bond network. This thesis investigates the relationship between structural water and proton intercalation in hydrated, layered tungsten oxides ($\text{WO}_3 \cdot 2\text{H}_2\text{O}$ and $\text{WO}_3 \cdot \text{H}_2\text{O}$) and compares their electrochemical behavior to anhydrous WO_3 . Bulk crystalline $\text{WO}_3 \cdot 2\text{H}_2\text{O}$, $\text{WO}_3 \cdot \text{H}_2\text{O}$, and WO_3 were synthesized via acid precipitation and subsequent thermal dehydration. Electrochemical behavior was characterized with three-electrode cyclic voltammetry in an acidic electrolyte. *In-situ* Raman spectroscopy was used to determine the

local structural and electronic changes of the materials during electrochemical cycling. These results show that all of the WO_3 phases undergo a semiconductor-to-metal transition upon proton intercalation. *Ex-situ* X-ray diffraction was used to study the structural changes of the materials after electrochemical cycling. It found that $\text{WO}_3 \cdot 2\text{H}_2\text{O}$ is largely preserved through electrochemical cycling with only a small decrease in capacity over 1000 cycles. While the total proton storage capacity of the hydrates was much lower than the anhydrate at slow cyclic voltammetry sweep rates, the capacities were nearly the same value at fast sweep rates. Kinetic analysis of the cyclic voltammetry data shows that the redox reaction was mainly diffusion controlled in WO_3 , while the reaction was capacitive in $\text{WO}_3 \cdot 2\text{H}_2\text{O}$. These results show that the presence of structural water in layered transition metal oxides leads to improved capacity retention at high rates, and the potential for high energy and high power density devices made with bulk redox active materials.

© Copyright 2016 William Chung Hei Lo

All Rights Reserved

Characterization of Hydrated Tungsten Oxides for Electrochemical Energy Storage.

by
William Chung Hei Lo

A thesis submitted to the Graduate Faculty of
North Carolina State University
in partial fulfillment of the
requirements for the degree of
Master of Science

Materials Science and Engineering

Raleigh, North Carolina

2016

APPROVED BY:

Dr. Veronica Augustyn
Committee Chair

Dr. Lewis Reynolds

Dr. Wei Gao

BIOGRAPHY

William Lo was born on June 20, 1992 in Hong Kong and grew up in Las Vegas, Nevada. Upon graduation from Advanced Technologies Academy, he attended Rose-Hulman Institute of Technology in Terre Haute, Indiana and obtained a Bachelor of Science degree in Physics and Mathematics with a minor in Chemical Engineering. Afterwards, he pursued a Master of Science degree at North Carolina State University under the direction of Dr. Veronica Augustyn.

ACKNOWLEDGEMENTS

First and foremost, I would like to thank my advisor, Dr. Veronica Augustyn, for her constant support and guidance throughout. Her passion for her research was truly an inspiration to me and everyone around her.

I also thank my thesis committee members Dr. Lewis Reynolds and Dr. Wei Gao for their evaluation of my research. Extra thanks goes out to Dr. Reynolds for his advice and thought-provoking discussions throughout.

I must also thank the fellow members of my group, Ruocun Wang and Shelby Boyd, for their frequent help, insights and discussions during this process.

Finally, I would like to thank my parents for their continuous and unconditional support throughout, which has made my entire career possible.

TABLE OF CONTENTS

List of Figures	vi
Chapter 1 – Introduction	1
1.1 Introduction and Motivation.....	1
1.2 Energy Storage	2
1.3 Hydrated Tungsten Oxide	9
Chapter 2 - Methods	12
2.1 Synthesis.....	12
2.2 Physical Characterization	13
2.3 Electrode Preparation	15
2.4 Electrochemical Setup.....	18
Chapter 3 – Results and Discussion	21
3.1 Synthesis.....	21
3.2 Physical Characterization	22
3.3 Electrochemical Characterization.....	25
3.4 <i>In-situ</i> and <i>Ex-situ</i> Characterization	35
Chapter 4 – Conclusions and Future Work	40
4.1 Conclusions	40
4.2 Future Work	41

References43

LIST OF FIGURES

Figure 1. Ragone plot comparing the power and energy densities of different EES devices ..	3
Figure 2. Schematic of a) an EDLC and b) the Stern model of the electric double layer	5
Figure 3. Schematic of a lithium-ion battery during discharge.....	7
Figure 4. Specific energies vs. charging time for a EDLC and a lithium ion battery	8
Figure 5. Polyhedral diagrams of a) $\text{WO}_3 \cdot 2\text{H}_2\text{O}$, b) $\text{WO}_3 \cdot \text{H}_2\text{O}$, c) WO_3	10
Figure 6. Flow chart for the synthesis of powder $\text{WO}_3 \cdot 2\text{H}_2\text{O}$	13
Figure 7. Schematic of the basic parts of a confocal microscope	15
Figure 8. Flow chart of the general method for creating a) bulk electrodes and b) screen printed electrodes	16
Figure 9. Pictures of the resulting a) slurry electrodes and b) screen printed electrodes created from the procedures outlined in Figure 8	17
Figure 10. a) Picture of the 3-electrode beaker cell setup used for electrochemical measurements and b) diagram of a 3 electrode cell.....	19
Figure 11. Picture of the setup used for in-situ Raman microscopy measurements	19
Figure 12. Picture of the as-synthesized $\text{WO}_3 \cdot 2\text{H}_2\text{O}$ powder from acid precipitation	21
Figure 13. TGA curve of $\text{WO}_3 \cdot 2\text{H}_2\text{O}$ powder.....	22
Figure 14. X-ray diffraction data for a) WO_3 , b) $\text{WO}_3 \cdot \text{H}_2\text{O}$, and c) $\text{WO}_3 \cdot 2\text{H}_2\text{O}$. with corresponding JCPDS reference files	23
Figure 15. Raman spectra showing distinct patterns for each hydration state of WO_3	24
Figure 16. Scanning electron micrographs of platelets of WO_3 at a) 20000x and b) 100000x	25

Figure 17. Cyclic voltammetry of the $\text{WO}_3 \cdot n\text{H}_2\text{O}$ materials at 2 mV/s in a) 0.5 M H_2SO_4 , b) 2 M Li_2SO_4 , c) 1 M Na_2SO_4 , and d) 0.5 M $\text{Mg}(\text{ClO}_4)_2$	26
Figure 18. Cyclic voltammetry of $\text{WO}_3 \cdot 2\text{H}_2\text{O}$ in 0.5 M H_2SO_4 , 2 M Li_2SO_4 , 1 M Na_2SO_4 , and 0.5 M $\text{Mg}(\text{ClO}_4)_2$ at 2 mV/s	27
Figure 19. Cyclic voltammetry of the $\text{WO}_3 \cdot n\text{H}_2\text{O}$ materials in 0.5 M H_2SO_4 at a) 2 mV/s, b) 20 mV/s, and c) 200 mV/s.	28
Figure 20. a) Gravimetric capacity, b) areal capacitance, and c) electrons stored per formula unit for each of the $\text{WO}_3 \cdot n\text{H}_2\text{O}$ materials	30
Figure 21. Kinetic analysis of the electrochemical energy storage behavior of WO_3	31
Figure 22. Kinetic analysis of the electrochemical energy storage behavior of $\text{WO}_3 \cdot 2\text{H}_2\text{O}$	32
Figure 23. Cyclic voltammetry of the 2nd and 1000th cycle in 0.5 M H_2SO_4 at 20 mV/s for a) WO_3 , b) $\text{WO}_3 \cdot \text{H}_2\text{O}$, and c) $\text{WO}_3 \cdot 2\text{H}_2\text{O}$	33
Figure 24. % capacity retention for the $\text{WO}_3 \cdot n\text{H}_2\text{O}$ materials at a) 20 mV/s and b) 200 mV/s in 0.5 M H_2SO_4	34
Figure 25. Self-discharge of the $\text{WO}_3 \cdot n\text{H}_2\text{O}$ materials over 12 hours, showing that the self-discharge rate increases as the amount of structural water increases.	35
Figure 26. Cyclic voltammetry of the screen printed electrodes at 1 mV/s in 0.5 M H_2SO_4 for a) $\text{WO}_3 \cdot 2\text{H}_2\text{O}$ b) $\text{WO}_3 \cdot \text{H}_2\text{O}$ c) $\text{WO}_3 \cdot \text{H}_2\text{O}$	37
Figure 27. In-situ Raman measurements for WO_3 taken every 100 mV during a linear sweep voltammetry experiment in 0.5 M H_2SO_4	37
Figure 28. In-situ Raman measurements for $\text{WO}_3 \cdot \text{H}_2\text{O}$ taken every 100 mV during a linear sweep voltammetry experiment in 0.5 M H_2SO_4	38

Figure 29. In-situ Raman measurements for $\text{WO}_3 \cdot 2\text{H}_2\text{O}$ taken every 100 mV during a linear sweep voltammetry experiment in 0.5 M H_2SO_4 38

Figure 30. Ex-situ XRD of $\text{WO}_3 \cdot n\text{H}_2\text{O}$ at open circuit potential and various cathodic potentials..... 39

CHAPTER 1 – Introduction

1.1 Introduction and Motivation

Global energy demands are expected to increase by nearly 40 percent by 2040.¹ At the same time, the ratio of fossil fuel usage to renewable energy usage is also projected to increase to meet the increased demand.² Renewable energy sources are the most promising sources of energy to replace fossil fuels as the primary fuel source. However, while energy can be retrieved from fossil fuels on demand, renewable energy sources such as solar and wind are subject to natural fluctuations in supply. The simplest solution for this problem is to store excess energy produced when conditions are optimal for renewable energy generation and to return this energy into circulation later when necessary. In addition to the large-scale energy storage required for grid usage, smaller scale energy storage is also required for portable applications such as electric cars and mobile phones. For both applications, a low-cost, safe, and long-lasting storage method is required for widespread implementation.

The motivation for this research is that the presence of structural water in bulk, layered oxide materials can facilitate rapid proton transport via the Grotthus mechanism. The goal of this research is to determine how structural water affects the kinetics of proton intercalation in hydrated tungsten oxide for electrochemical energy storage. Hydrated tungsten oxides are model materials for this research because they are crystalline, easily synthesized, redox-active, and stable in both aqueous and non-aqueous electrolytes. Specifically, tungsten oxide dihydrate ($\text{WO}_3 \cdot 2\text{H}_2\text{O}$) was synthesized by acid precipitation and then dehydrated into the monohydrate ($\text{WO}_3 \cdot \text{H}_2\text{O}$) and anhydrate (WO_3) forms. From there, electrodes were fabricated by painting a carbon paper substrate with slurries made from a mixture of the tungsten oxide active material, acetylene black, and polyvinylidene fluoride. The slurry electrodes were used to measure the

materials' charge storage capacity, kinetics, and stability via three-electrode cyclic voltammetry in an acidic electrolyte. *Ex-situ* X-ray diffraction measurements were taken to determine whether structural changes occurred after electrochemical cycling. *In-situ* Raman spectroscopy was performed in order to detect local structural and electronic changes in the materials during electrochemical cycling.

1.2 Energy Storage

The main types of energy storage are mechanical, electrical, chemical, and electrochemical. Though there are several different forms of mechanical energy storage, such as compressed air and flywheel, the only widespread use of mechanical energy storage is with hydroelectric dams.³ These are expensive, adversely affect the environment around them, and are subject to reduced output during times of severe drought.⁴ Electrical energy storage in the form of dielectric capacitors, where energy is stored electrostatically, has the fastest response times but suffers from anemically low storage capacity due to limited surface areas and physical constraints on the minimum separation distance between the capacitor plates.⁵ Recently, there has been success in improving the charging rate and energy density of dielectric capacitors by using a mixed RC circuit, where a resistor and a resistor-capacitor pair work in parallel to facilitate charging, which is then switched to a resistor to dam the charge for long-term storage.⁶ Chemical energy storage, whereby energy is stored in chemical bonds, offers significantly higher energy densities. The most familiar chemical energy storage are fossil fuels, but these are produced over millions of years. More practical forms of chemical energy storage include hydrogen and biofuel, but both of these suffer from drawbacks. The primary challenge for hydrogen fuel is from the production side, where the main method is steam

reformation of natural gas which produces carbon dioxide as a by-product and thus is counterproductive for a clean energy economy.⁷ In addition, while fuel cell technologies are adequately mature for implementation of hydrogen fuels, mass distribution of hydrogen is difficult due insufficient infrastructure.⁸ Biofuels are theoretically carbon-neutral fuels, but production is limited by the amount of feedstock available for conversion which requires the use of large land areas.⁹ Electrochemical energy storage (EES) is one of the most promising methods for energy storage, due to its high efficiency and the range of power and energy densities (**Figure 1**) which can enable a variety of applications.¹⁰ In addition, EES devices are modular and can be adapted for large scale grid applications or small scale microelectronics.

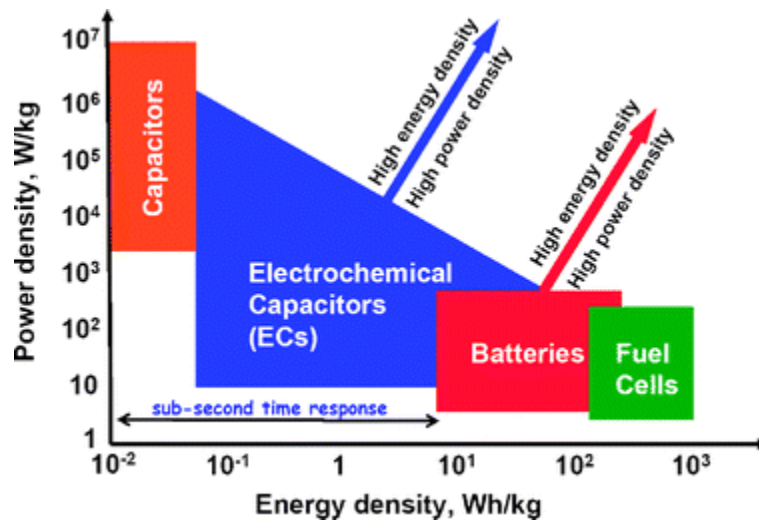


Figure 1. The Ragone Plot shows the relationship between power and energy density for different EES devices.¹⁰ A major driving force for EES research is to simultaneously improve both energy and power density, as indicated by arrows.

The simplest type of EES is the electric double layer capacitor (EDLC). Energy storage in EDLCs involves no charge transfer reactions.¹¹ Conceptually, this mechanism is like that of a dielectric capacitor, where opposite charges accumulate on conductive plates, and energy is stored due to the separation of charge. The defining characteristic of a capacitor is the capacitance, which reflects the charge storage ability of the device, and is defined by:

$$C = \frac{\epsilon A}{d} \quad (1.1)$$

where C is the capacitance, A is the surface area of each plate, d is the separation between the plates, and ϵ is the permittivity of the dielectric medium.

EDLCs exhibit much higher capacitances than dielectric capacitors because of the large surface areas of the electrode materials and very small separation distances (on the order of Ångstroms) both of which increase the capacitance, as shown by Equation 1.1. Typical materials used for EDLCs are high surface area ($> 1,000 \text{ m}^2/\text{g}$) carbons, which exhibit capacitances of up to 150 F/g .^{12–14} Since the energy storage of capacitors involves only surface adsorption and not chemical or phase changes in the bulk of the electrode material, EDLCs typically have lifetimes of up to 1,000,000 cycles and are highly reversible devices.¹¹ **Figure 2a** shows a diagram of a typical charged EDLC, where the electrolyte could be either aqueous or non-aqueous, and the electrodes are high surface area, porous carbon materials that maximize the electrolyte/electrode interfacial area.

The mechanistic description of EDLC energy storage is shown in **Figure 2b**, in a schematic of the Stern model of the electric double layer at an electrode interface. The layer closest to the electrode is called the Stern layer, in which ions are considered to have finite size. Unsolvated anions reside closest to the electrode, in the inner Helmholtz plane (IHP), whereas adsorbed solvated cations reside in the outer Helmholtz plane (OHP). Past the OHP

is a diffuse layer where the ions are distributed according to the Maxwell-Boltzmann distribution. The major change in potential, ψ , is across the Stern layer. Since the distance across this layer is very small (on the order of Ångstroms), and the interfacial area is large, this leads to the large capacitances of carbon materials used for EDLCs.

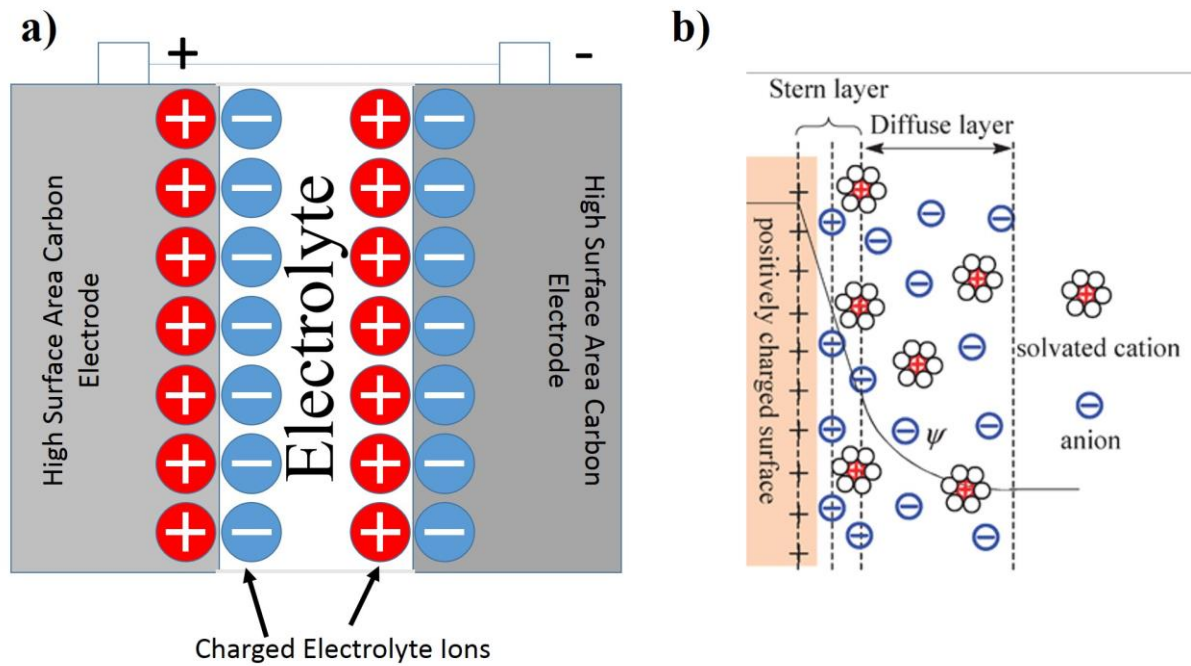


Figure 2. a) Schematic of an EDLC during the charging stage, where electrolyte ions electrostatically adsorb at the surface of high surface area carbon electrodes, and b) Schematic of the Stern model of the electric double layer, adapted from Reference 5.

Secondary (rechargeable) batteries are EES devices that are prolific throughout the world because they are commonly used in mobile devices and vehicles. In contrast to EDLCs, batteries undergo Faradaic charge transfer reactions in order to store energy. In addition, battery electrodes store charge in the bulk and generally undergo phase changes, so that the

kinetics are limited by solid-state diffusion, leading to lower power densities when compared to other EES devices.^{11,15} As a result of the electrode material undergoing phase changes during charging and discharging, the lifetime of batteries (< 1,000 cycles) is significantly lower than that of capacitors, which can undergo up to 1,000,000 cycles.¹¹ Lithium-ion batteries are the most common batteries for electric vehicles and portable electronics. Commercial lithium-ion batteries consist of a cathode, typically LiCoO₂, and an anode, typically graphite, with lithium ions intercalating in and out of the electrodes during the charging and discharging process. The reactions occurring at the cathode and anode (discharge in the forward direction, charge in the reverse direction) are:

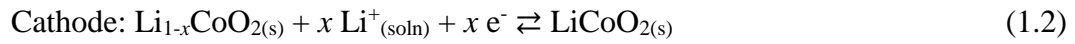


Figure 3 shows the schematic of a typical lithium-ion battery during discharge.

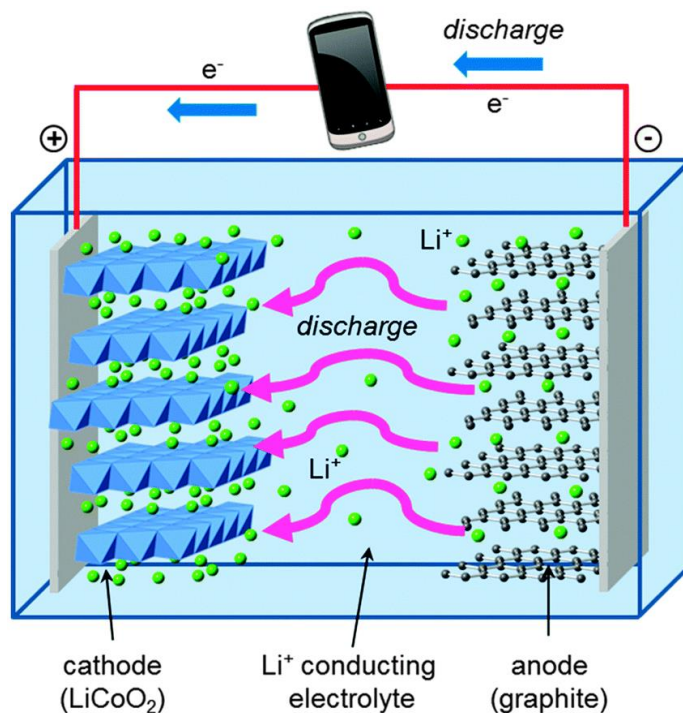


Figure 3. Schematic of a typical lithium-ion battery during discharge. Reproduced from Reference 17.

Pseudocapacitance is an EES mechanism in between that of batteries and EDLCs. The use of pseudocapacitance in electrochemical capacitors can offer higher energy densities than EDLCs and higher power densities than batteries.¹⁶ **Figure 4** compares the specific energy and power of a thin film lithium-ion battery with that of an EDLC.¹⁷ The empty region between the relatively flat capacitive response of the EDLC and the plateau of the battery, corresponding to charge/discharge times from about 10 seconds to nearly 10 minutes, is the region where pseudocapacitors can outperform currently available devices.¹⁸ In pseudocapacitive materials, energy is stored via Faradaic reactions, but the kinetic behavior resembles that of a capacitive material. There are three types of pseudocapacitive mechanisms possible in electrochemical systems: (1) underpotential deposition, where a monolayer of metal

ions are adsorbed onto the surface of a different metal; (2) intercalation pseudocapacitance, where the electrode is a host for ion intercalation and subsequent faradaic reaction but with no accompanying phase change; and (3) redox pseudocapacitance, where ions adsorb on an electrode surface and are accompanied by a Faradaic reaction on the electrode.¹¹ Pseudocapacitance is a promising mechanism to simultaneously improve both energy and power density of a material, as has been demonstrated for nanostructured oxides.¹⁸ The purpose of this research is to determine whether a pseudocapacitive mechanism is possible in bulk, hydrated and layered oxide materials.

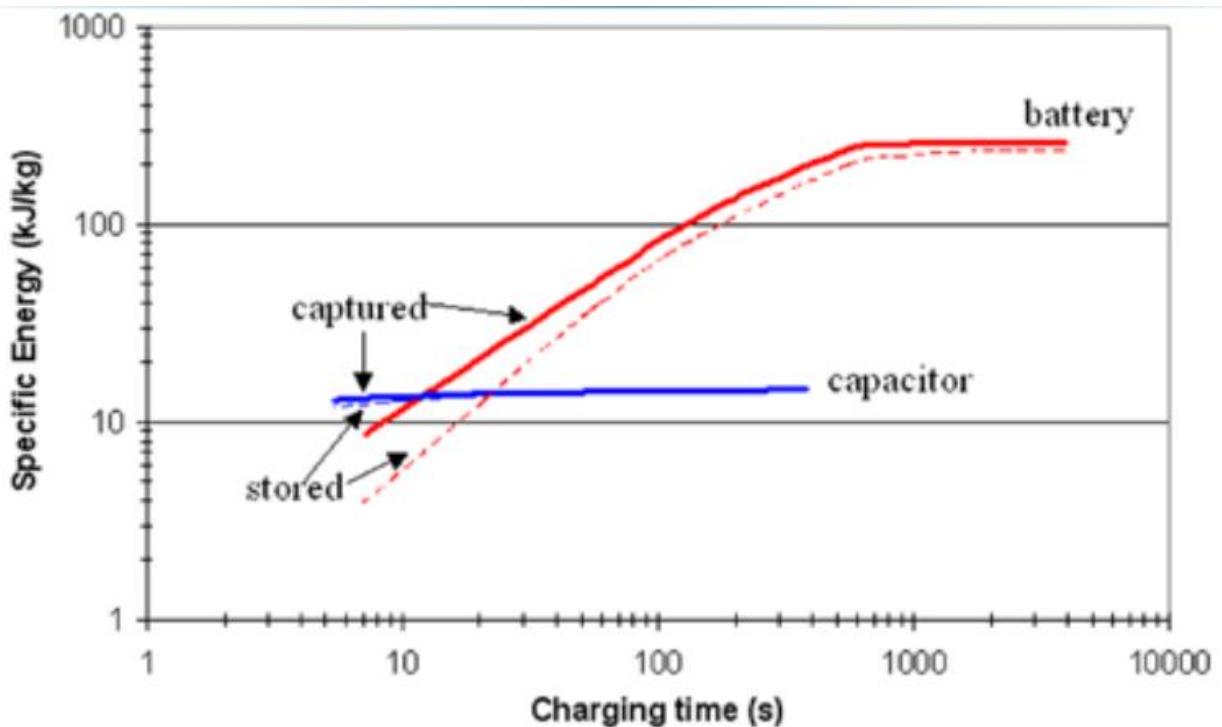
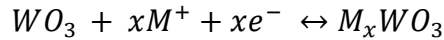


Figure 4. Specific energy vs. charging time for a EDLC and a thin film lithium ion battery.¹⁷

The battery exhibits a decrease in the specific energy with charging time due to slow kinetics, while the EDLC provides a constant but low specific energy with charging time because the energy storage mechanism is electrostatic.

1.3 Hydrated Tungsten Oxides

Various transition metal oxides can exhibit pseudocapacitive behavior, including MnO_2 , $\text{RuO}_2 \cdot x\text{H}_2\text{O}$, and MoO_{3-x} .¹⁹⁻²² Tungsten oxide (WO_3) is an n-type semiconductor and can easily be tuned between its dihydrate, monohydrate, and anhydrate crystal structures by simple dehydration.^{23,24} Traditionally, tungsten oxide has been studied as a material for electrochromic devices.²⁵⁻²⁷ In electrochromic devices, the formal charge of the tungsten changes with intercalation of protons or alkali metal ions, which produces a corresponding color change from yellow to blue. This is due to the change in the band gap of the material by the intercalation reaction:²⁸



where M is either a proton or an alkali metal ion such as Li^+ , and x is ≤ 1 . Electrochemical intercalation involves the insertion of an ion from the electrolyte into a vacant site of a solid state structure with concomitant electron transfer from the external circuit. Since the electrochromic coloration mechanism is due to the same electrochemical reaction as energy storage, tungsten oxide has become of interest as a possible energy storage material. The intercalation of 1 alkali cation or proton leads to a maximum theoretical capacity of 416 C/g or 116 mAh/g in WO_3 .²⁹

$\text{WO}_3 \cdot 2\text{H}_2\text{O}$ is a layered oxide material, with each tungsten in an octahedral coordination by oxygen, as seen in **Figure 5a**. One type of water molecule resides in the interlayer spacing, and the second type of water molecule is directly coordinated to tungsten at the top or bottom of the octahedron. During dehydration to the monohydrate phase at 120°C (**Figure 5b**), the interlayer water molecules are removed, and only the coordinated water molecules remain. Finally, heat treatment of the dihydrate at 350°C leads to the formation of

anhydrous WO_3 , where all of the water is removed from the structure, leaving behind corner sharing octahedrons in a distorted ReO_3 structure (**Figure 5c**).³⁰

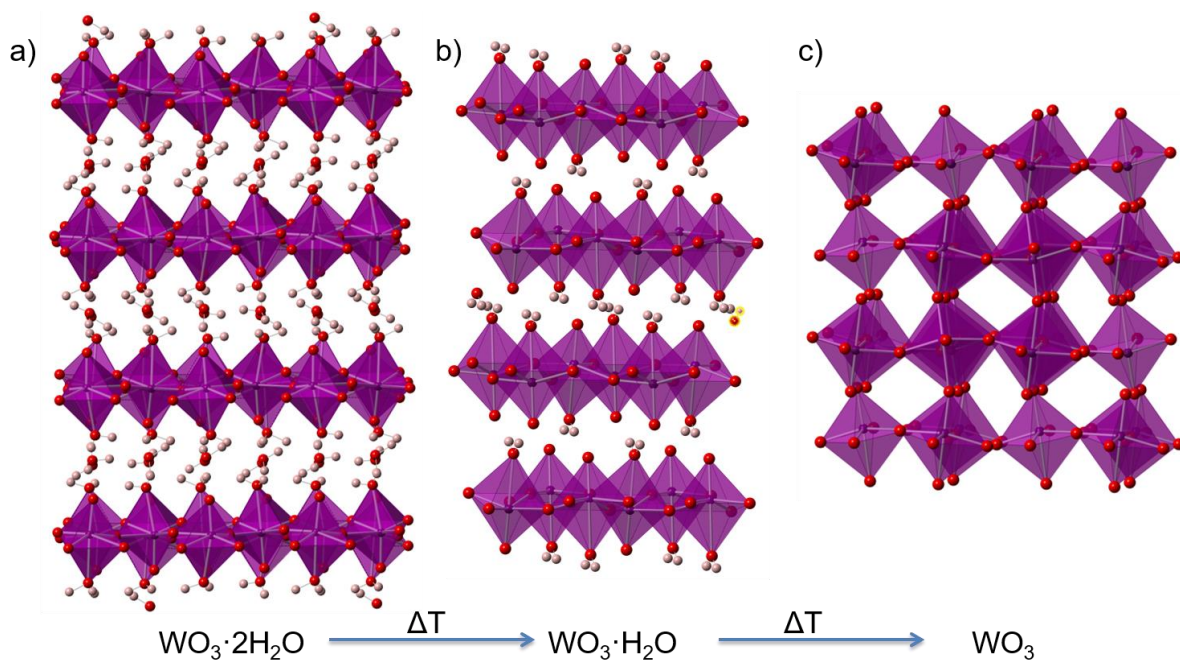


Figure 5. Crystal structures of a) $\text{WO}_3 \cdot 2\text{H}_2\text{O}$, b) $\text{WO}_3 \cdot \text{H}_2\text{O}$, and c) WO_3 . The monohydrate and anhydrate phases are obtained by dehydration of $\text{WO}_3 \cdot 2\text{H}_2\text{O}$ at less than 350°C in air.

To explain the high ionic conductivity of protons in water, Grotthuss proposed a transport mechanism whereby the proton jumps from water molecule to water molecules via hydrogen bonding.³¹ Since then, the concept has been extended to molecular structures containing water, and though the specifics of the mechanism are still debated, improved proton transport has been attributed to the presence of structural water in hydrous RuO_2 , Sb_2O_3 , SnO_2 , ZrO_2 , and graphite, among others.^{32–35} In WO_3 hydrates, it was found that at intermediate temperatures, the dihydrate exhibited proton conductivity an order of magnitude higher than

the monohydrate, suggesting that proton diffusion through tungsten oxide could be mediated by the Grotthuss mechanism like in other hydrous materials.³⁶ However, density function theory calculations have shown that this may not be the case in tungsten oxide, and proton diffusion in the dihydrate and anhydrate actually occurs via the octahedral layers.³⁷ If structural water does indeed facilitate diffusion of protons in hydrated WO_3 , then the rate capability of the hydrated oxides should be faster than that of the anhydrous oxides. Furthermore, due to the large interlayer spacing created by the water molecules, the lifetime of the hydrated WO_3 should be greater than that of anhydrous WO_3 .

Chapter 2 - Methods

2.1 Synthesis

The acidic precipitation reaction described by Freedman (shown in **Figure 6**) was used to synthesize $\text{WO}_3 \cdot 2\text{H}_2\text{O}$, which also served as the precursor for $\text{WO}_3 \cdot \text{H}_2\text{O}$ and WO_3 .³⁸ Briefly, 50 mL of a 1M aqueous $\text{Na}_2\text{WO}_4 \cdot 2\text{H}_2\text{O}$ (Sigma Aldrich) solution was added dropwise at a rate of ~1 drop/second into 450 mL of stirred 3M HCl. Almost immediately, a yellow precipitate appeared and continued to precipitate throughout the entire time that sodium tungstate was added to the acid. After addition of all of the sodium tungstate, the solution was aged for an hour and rinsed until the solution was at a neutral pH as indicated by litmus paper. The obtained $\text{WO}_3 \cdot 2\text{H}_2\text{O}$ precipitate was filtered, dried in an oven at 50°C, and then ground into a fine powder with a mortar and pestle. To obtain $\text{WO}_3 \cdot \text{H}_2\text{O}$ and WO_3 , the $\text{WO}_3 \cdot 2\text{H}_2\text{O}$ was dried in an oven at, respectively, 120° or 350° in air.

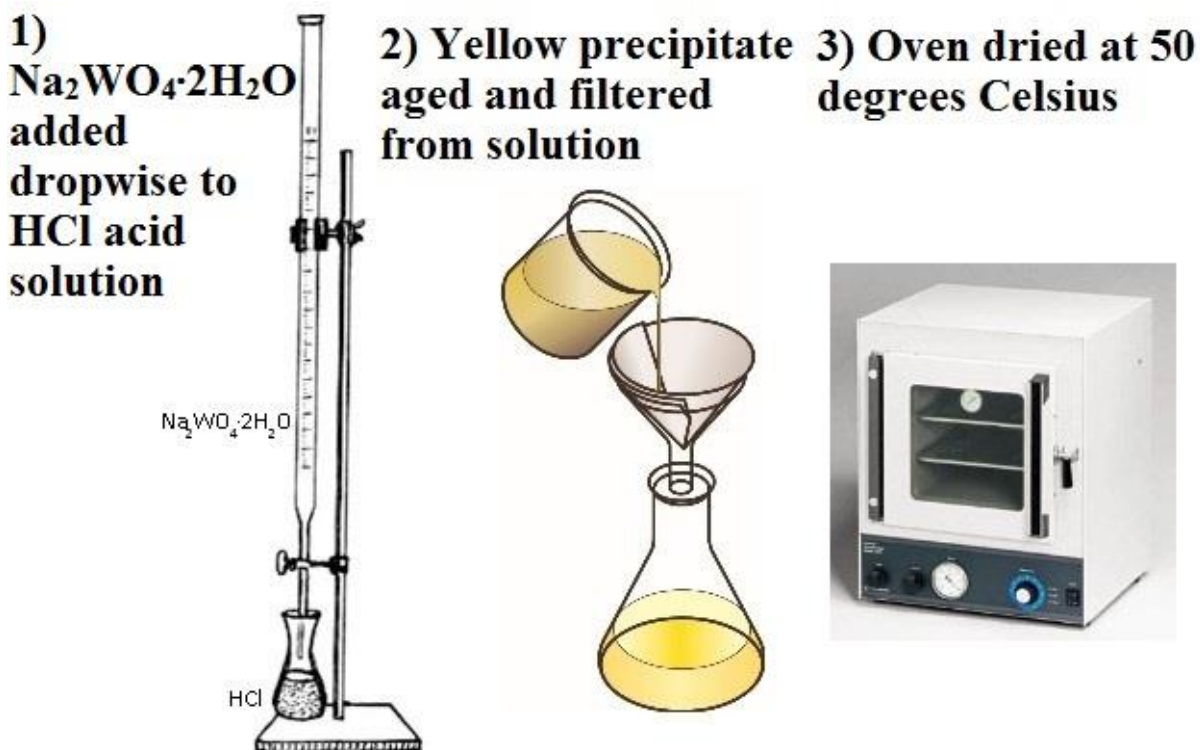


Figure 6. Flow chart for the synthesis of bulk, layered $\text{WO}_3 \cdot 2\text{H}_2\text{O}$. The synthesis follows the method developed by Freedman.³⁸

2.2 Physical Characterization

Physical characterization of the synthesized materials was performed with X-ray diffraction (XRD), Raman spectroscopy, thermogravimetric analysis (TGA), and scanning electron microscopy (SEM).

XRD was used to determine the phase and crystallinity of the as-synthesized powder, as well as the dehydrated powders. It was performed on a Rigaku SmartLab X-ray diffractometer in a standard Bragg-Brentano geometry. *Ex-situ* XRD was performed on electrochemically cycled WO_3 , $\text{WO}_3 \cdot \text{H}_2\text{O}$, and $\text{WO}_3 \cdot 2\text{H}_2\text{O}$ electrodes in order to determine whether electrochemical cycling had affected the structure of the materials.

A WiTEC alpha300R confocal Raman microscope was used for Raman spectroscopy in order to identify the local structure of synthesized materials and for *in-situ* characterization during electrochemical energy storage in an acidic electrolyte. The laser wavelength was 532 nm and a 10X objective was used. A typical confocal microscope system is depicted in **Figure 7**. Confocal microscopy in conjunction with Raman spectroscopy allows the acquisition of a Raman spectrum at specific depths into the samples by filtering out all excess light using a pinhole, whereas conventional microscopy would capture information from as far as the laser light can penetrate. Raman microscopy lends itself to *in-situ* characterization of EES materials because the focal plane can be selected so as to exclude the electrolyte, and the measurement is performed in ambient atmosphere.

TGA was used to determine the temperatures required for dehydration of the $\text{WO}_3 \cdot 2\text{H}_2\text{O}$ precursor powder into the monohydrate and anhydrate phases of WO_3 . A Seiko Exstar TG/DTA6200 was used to perform TGA of the as-synthesized sample. The measurement was performed using 20 mg of $\text{WO}_3 \cdot 2\text{H}_2\text{O}$ powder from room temperature up to 500°C , with a nitrogen flow rate of $150 \text{ cm}^3/\text{min}$ to ensure sufficient flow of oxygen out of the chamber.

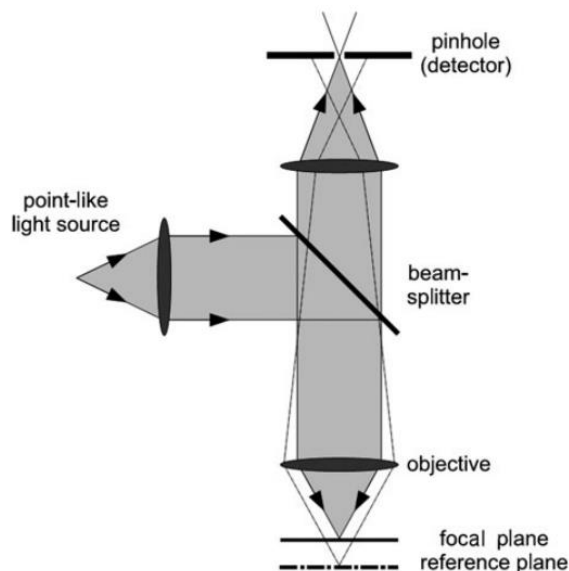


Figure 7. Schematic of the basic parts of a confocal microscope. The confocal setup converges the light source on the focal plane in order to increase spatial resolution by limiting the depth of focus.³⁹ This mechanism is responsible for the high resolution of Raman microscopy, used in this thesis for characterization of the local material structure and *in situ* measurements.

SEM was used to determine the microstructure of the synthesized powders and the electrodes fabricated from the powders. SEM was performed with a field emission FEI Verios 460L.

2.3 Electrode Preparation

In order to fabricate electrodes for electrochemical analysis, the active material must be blended with a mixture of acetylene black and polyvinylidene fluoride (PVDF). The acetylene black serves as the conductive additive to improve electron transport throughout the electrode. Without it, the electrode would be too resistive and electrons would not be able to

reach the electrochemical interface. PVDF serves as the binder to hold together the acetylene black, the active material, and the conductive substrate (also known as the current collector). The slurry mixture is 80 wt% active material ($\text{WO}_3 \cdot 2\text{H}_2\text{O}$, $\text{WO}_3 \cdot \text{H}_2\text{O}$, or WO_3), 10 wt% acetylene black, and 10 wt% PVDF in n-methylpyrrolidone (NMP), a common aprotic solvent. The weight percentages are chosen to minimize the amount of PVDF or acetylene black while maintaining electrode stability and conductivity. The slurry was pasted onto a carbon paper current collector and dried at 50°C in air. The carbon paper was chosen because it is stable in highly acidic electrolytes and provides minimal background current. The final mass loading was $\sim 1 \text{ mg}$ of $\text{WO}_3 \cdot n\text{H}_2\text{O}$ per cm^2 . **Figure 8a** shows the flow chart of the method for fabricating slurry electrodes of $\text{WO}_3 \cdot n\text{H}_2\text{O}$ for three-electrode cyclic voltammetry.

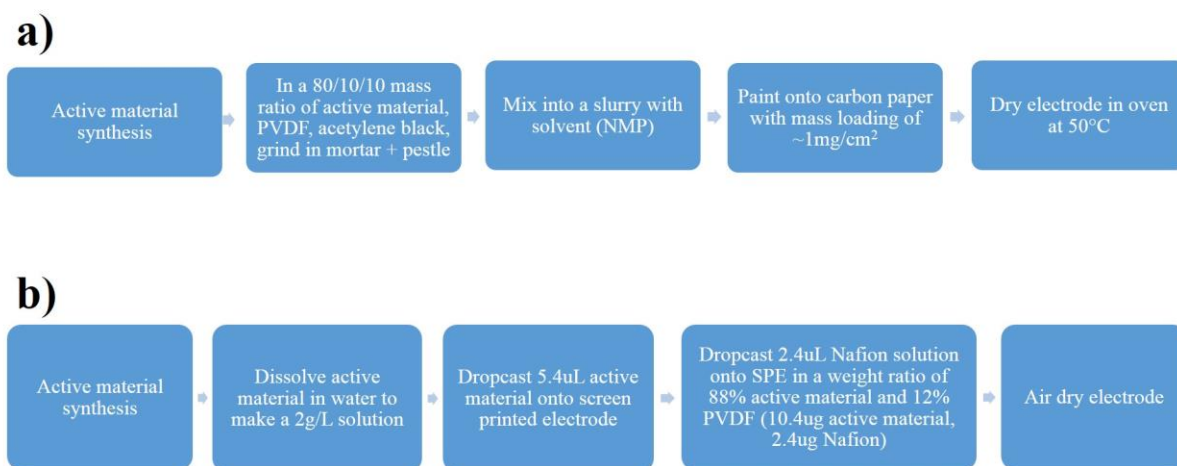


Figure 8. Flow chart of methods for fabricating $\text{WO}_3 \cdot n\text{H}_2\text{O}$ electrodes: a) slurry-cast electrodes for three-electrode cyclic voltammetry and b) screen printed electrodes for *in situ* Raman measurements.

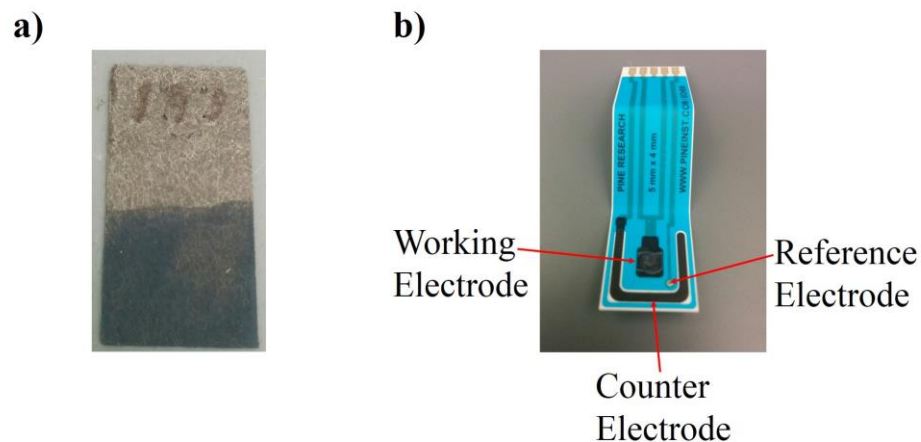


Figure 9. Pictures of the a) slurry-cast electrodes and b) screen printed electrodes fabricated using the methods outlined in Figure 8.

Different electrodes are necessary for performing the *in-situ* Raman spectroscopy in order to accommodate the electrochemical cell underneath the microscope objective. **Figure 8b** details the general method for creating electrodes for this measurement, where the active material powder is dispersed in water (2 g of $\text{WO}_3 \cdot n\text{H}_2\text{O}/\text{L}$), dropcast onto a paper screen printed electrode (Pine Instruments), stabilized on the electrode using a layer of Nafion, and then air dried. Nafion is a proton-conductive sulfonated fluoropolymer and was used as a solution (5 wt% in alcohol, Fuel Cell Earth). Since the active material mass loading is low ($66 \text{ ug}/\text{cm}^2$), a conductive additive is not needed. After experimenting with both PVDF and Nafion as a binder for screen printed electrodes, it was found that Nafion preserved more material after cycling.

2.4 Electrochemical Setup

Electrochemical characterization was performed in a three electrode cell, which was used in order to accurately measure the potential and current through the electrode. The setup shown in **Figure 10a** was used in conjunction with a Biologic VMP3 potentiostat to perform cyclic voltammetry. The reference electrode was Ag/AgCl in saturated KCl solution (Pine Instruments) and the counter electrode was Pt wire (99.997%, Alfa Aesar). The slurry-cast working electrode and counter electrode are connected to the external circuit using alligator clips soldered to copper wire. Four different aqueous electrolytes were used (0.5 M H₂SO₄, 2 M Li₂SO₄, 1 M Na₂SO₄, and 0.5 M Mg(ClO₄)₂) in order to determine the effect of cation size and pH on the electrochemical behavior of the WO₃·*n*H₂O materials.

Figure 10b shows the schematic of a three electrode cell, where the current flows between the working and counter electrode and the potential is measured between the working and reference electrodes.⁴⁰ In this way, the potential of the working electrode during electrochemical cycling can be referenced to a stable potential. All potentials are referenced vs. the saturated Ag/AgCl electrode (0.198 V vs. SHE, standard hydrogen electrode). The three-electrode cell was also used for linear sweep experiments to drive the electrode to a desired potential for *ex-situ* XRD measurements.

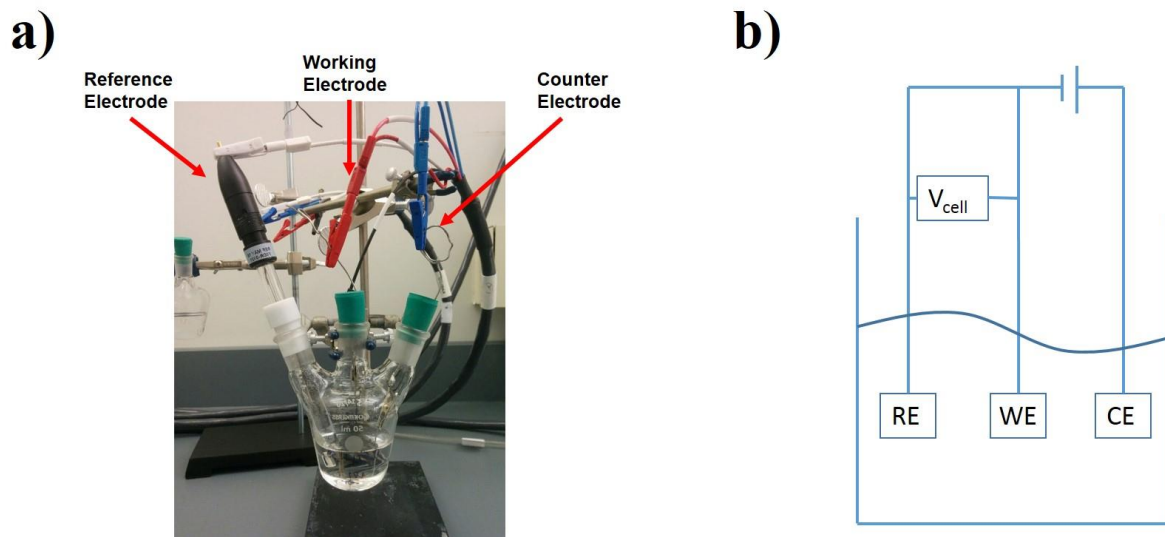


Figure 10. a) Picture of the three-electrode cell used for electrochemical measurements and b) schematic diagram of a three-electrode cell.

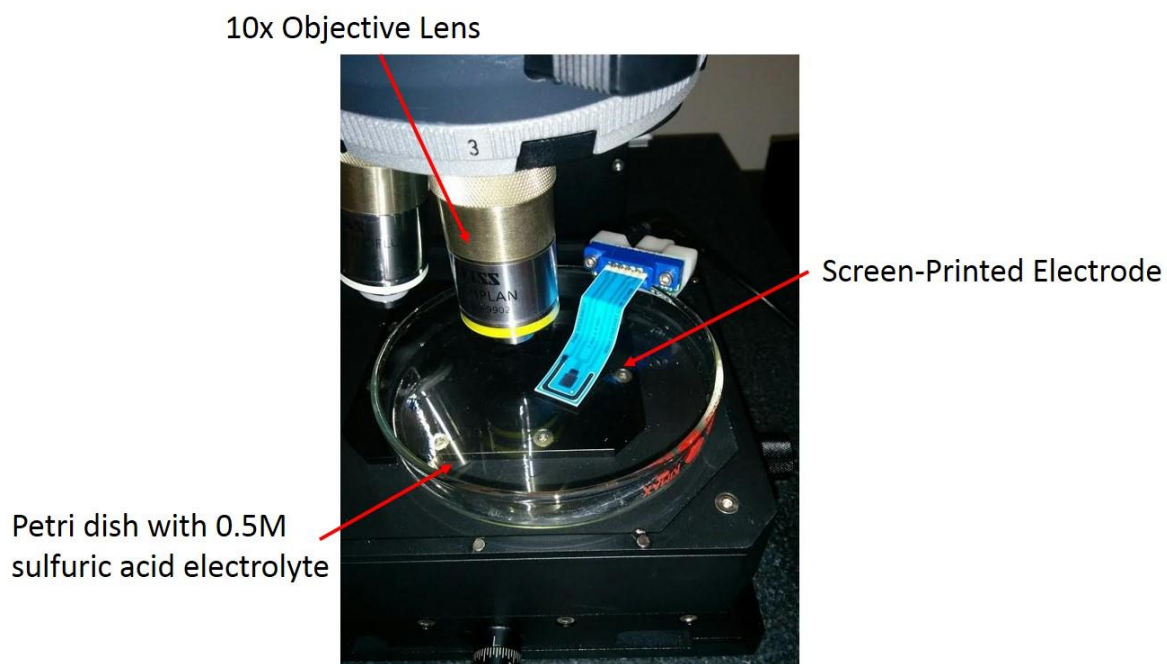


Figure 11. Picture of the setup used for *in-situ* Raman microscopy measurements.

For *in-situ* Raman microscopy, a screen printed electrode was taped onto a Petri dish filled with ~ 1 cm of 0.5 M H₂SO₄ electrolyte (**Figure 11**). The end of the screen printed electrode was connected to a Pine Instruments WaveNow potentiostat. In confocal Raman microscopy, the laser can easily be focused through the solution to minimize the electrolyte contribution to the Raman spectrum.

Chapter 3 – Results and Discussion

3.1 Synthesis

The acid precipitation method described by Freedman was used to prepare $\text{WO}_3 \cdot 2\text{H}_2\text{O}$.³⁸ The product of the precipitation synthesis is a bright yellow powder (**Figure 12**), indicative of tungsten in the 6^+ oxidation state.

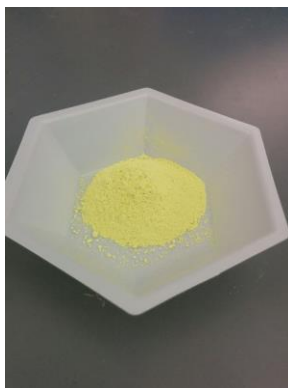


Figure 12. Picture of the as-synthesized $\text{WO}_3 \cdot 2\text{H}_2\text{O}$ powder from acid precipitation, showing the distinctive yellow color of tungsten in the 6^+ state.

TGA was used to determine the heat treatment temperature required for the dehydration of $\text{WO}_3 \cdot 2\text{H}_2\text{O}$ to $\text{WO}_3 \cdot \text{H}_2\text{O}$ and WO_3 . **Figure 13** displays the percentage weight loss of the $\text{WO}_3 \cdot 2\text{H}_2\text{O}$ with increasing temperature. The two distinct weight loss steps correspond to the removal of structural water molecules. From the TGA data, it was determined that to synthesize $\text{WO}_3 \cdot \text{H}_2\text{O}$ and WO_3 , the $\text{WO}_3 \cdot 2\text{H}_2\text{O}$ powder would have to be dehydrated at 120°C and 350°C , respectively.

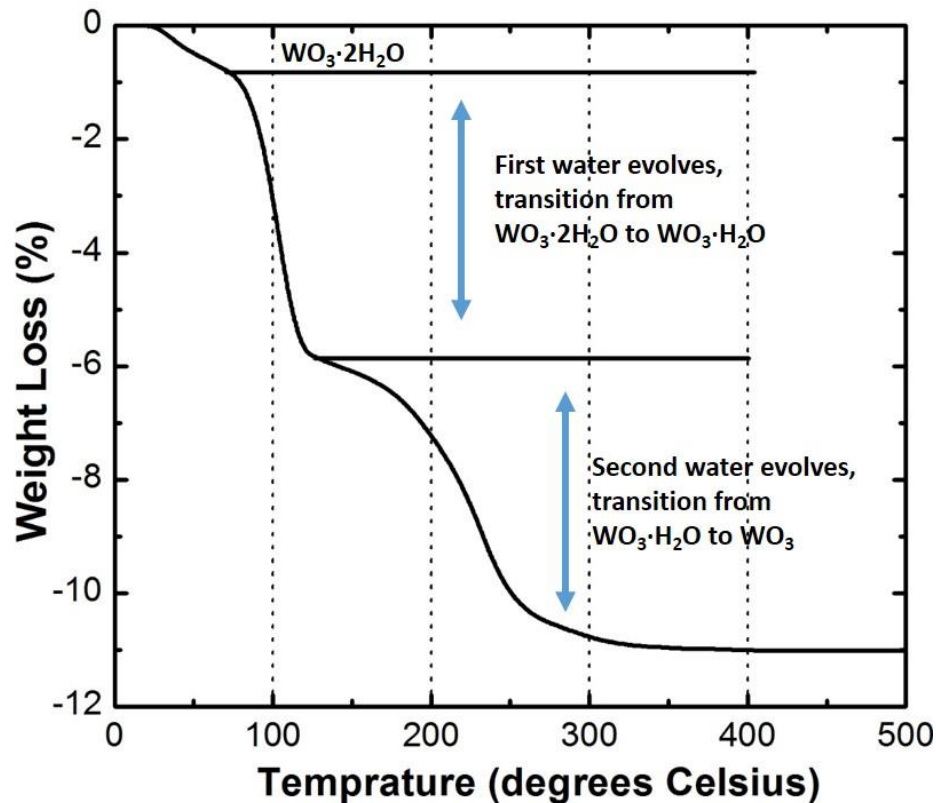


Figure 13. TGA curve of $\text{WO}_3 \cdot 2\text{H}_2\text{O}$ powder shows two distinct weight loss steps, which correspond to the removal of structural water, and formation of monohydrate at 120°C and anhydrate at 350°C .

3.2 Physical Characterization

After dehydration in an oven at the specified temperatures for the synthesis of $\text{WO}_3 \cdot \text{H}_2\text{O}$ and WO_3 , X-ray diffraction (XRD) measurements were taken in order to determine the crystallinity and phase purity. **Figure 14a, b, and c** shows the XRD measurements for WO_3 , $\text{WO}_3 \cdot \text{H}_2\text{O}$, and $\text{WO}_3 \cdot 2\text{H}_2\text{O}$, respectively, with corresponding JCPDS reference files underneath. The sharp peaks for each hydration state indicate the high crystallinity for all samples, even after dehydration. The obtained materials are phase-pure, including no

impurities from other hydrated phases. The hydrated WO_3 are layered compounds, with an interlayer spacing of 6.96 Å for $\text{WO}_3 \cdot 2\text{H}_2\text{O}$ and 5.36 Å for $\text{WO}_3 \cdot \text{H}_2\text{O}$.

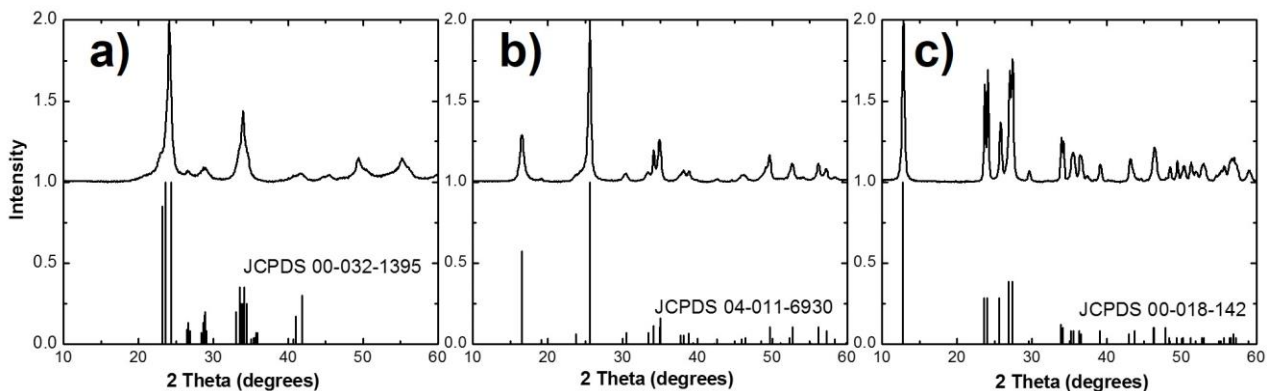


Figure 14. XRD of a) WO_3 , b) $\text{WO}_3 \cdot \text{H}_2\text{O}$, and c) $\text{WO}_3 \cdot 2\text{H}_2\text{O}$. The corresponding JCPDS reference spectra for each phase are shown below the experimental results.

In addition to XRD, Raman spectroscopy was used to distinguish between the three phases. **Figure 15** shows overlaid spectra of all three $\text{WO}_3 \cdot n\text{H}_2\text{O}$ phases. In all of the materials, the peaks at $< 100/\text{cm}$ correspond to lattice modes. In the hydrated forms, the peaks around 200-400 correspond to the bending of the O-W-O bonds, and the broad peaks at about 700/cm correspond to the stretching of the O-W-O bonds. The peak at 950/cm is indicative of hydrated WO_3 and corresponds to the stretching of the terminal W=O bond.⁴¹

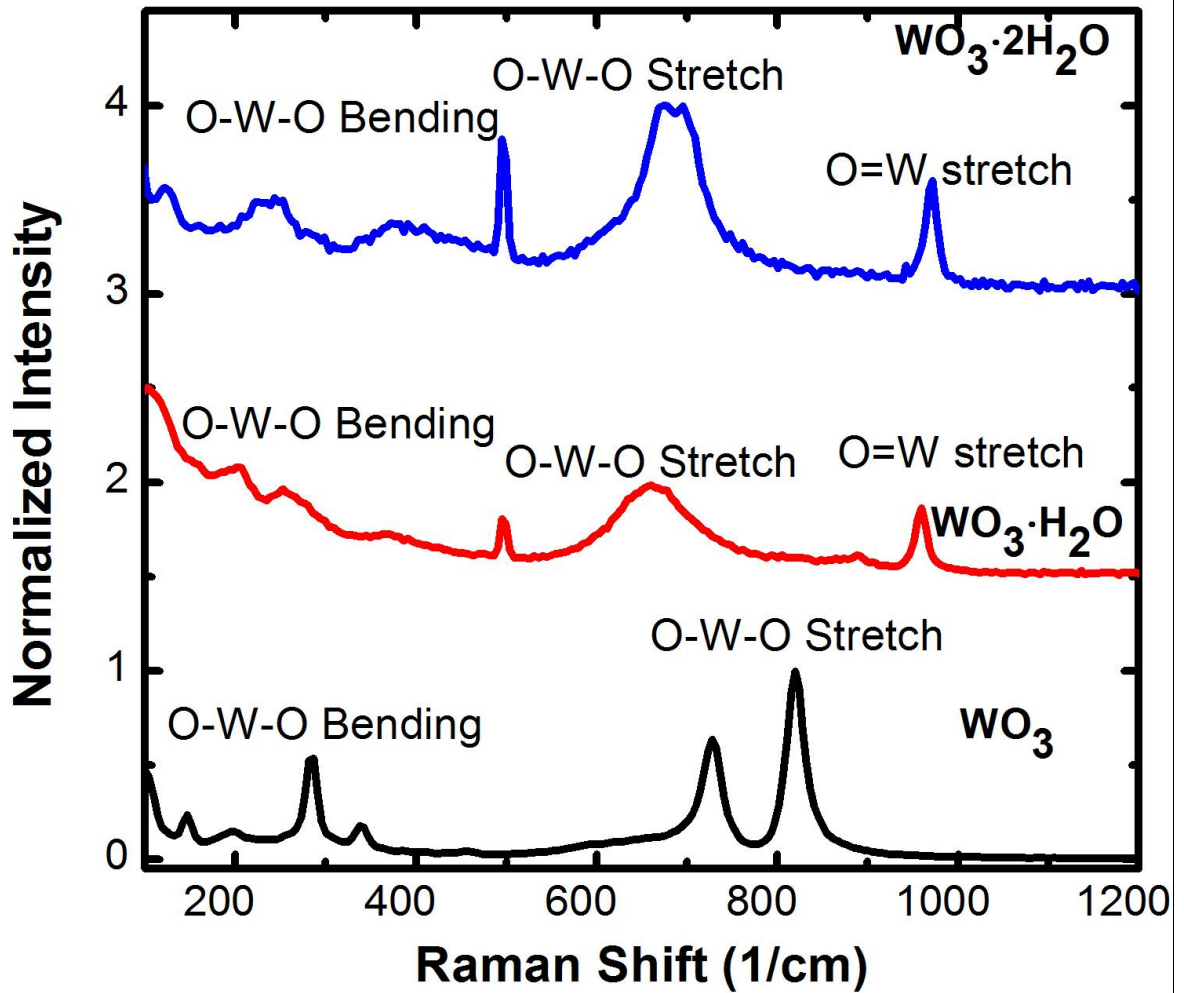


Figure 15. Raman spectra showing distinct patterns for the three $\text{WO}_3 \cdot n\text{H}_2\text{O}$ phases. The peak at $\sim 950 \text{ cm}^{-1}$ can be used to distinguish the hydrated phases from the anhydrous phase, while the double peak for O-W-O stretching is indicative of the anhydrous phase.

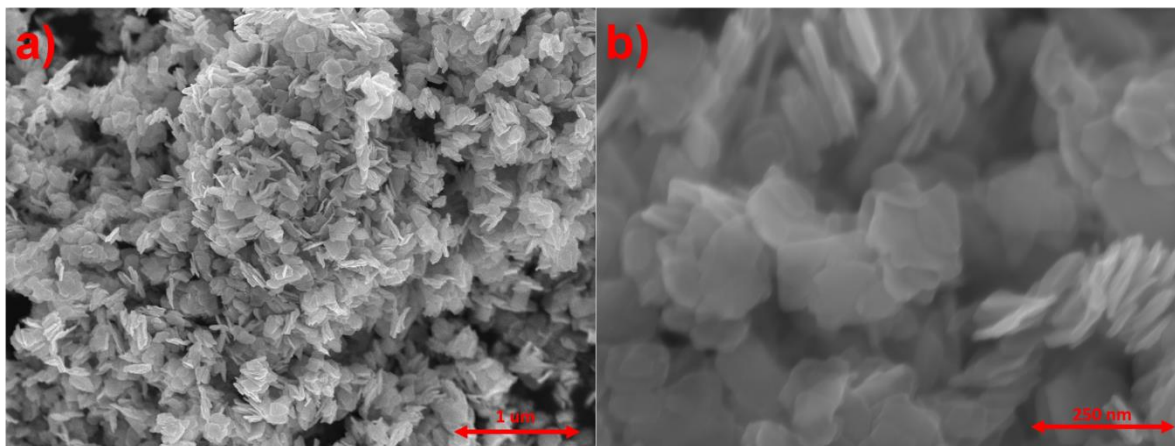


Figure 16. SEM micrographs of platelets of WO_3 at a) 20000x and b) 100000x. The plate-like morphology is indicative of the layered structure of the precursor material.

SEM (**Figure 16**) reveals the morphology of the synthesized WO_3 powder to be plate-like, even after dehydration, which is reminiscent of the layered structure of the precursor $\text{WO}_3 \cdot 2\text{H}_2\text{O}$. Most plates appear to be about 200 nm wide, with a thickness of about 10 nm.

3.3 Electrochemical Characterization

Three-electrode cyclic voltammetry was performed at various sweep rates in four electrolytes (0.5 M H_2SO_4 , 2 M Li_2SO_4 , 1 M Na_2SO_4 , and 0.5 M $\text{Mg}(\text{ClO}_4)_2$) in order to determine the effect of cation size and electrolyte pH on the energy storage behavior of the three $\text{WO}_3 \cdot n\text{H}_2\text{O}$ phases. **Figure 17** shows the electrochemical behavior of the anhydrous and hydrated WO_3 in each of these electrolytes. From these figures and from **Figure 18**, which compares $\text{WO}_3 \cdot 2\text{H}_2\text{O}$ CVs in all 4 electrolytes, it can be seen that all three $\text{WO}_3 \cdot n\text{H}_2\text{O}$ phases are not very active in the neutral pH electrolytes because the current density is lower than in

the H_2SO_4 electrolyte. As a result, the remainder of the electrochemical characterization was performed in 0.5 M H_2SO_4 electrolyte.

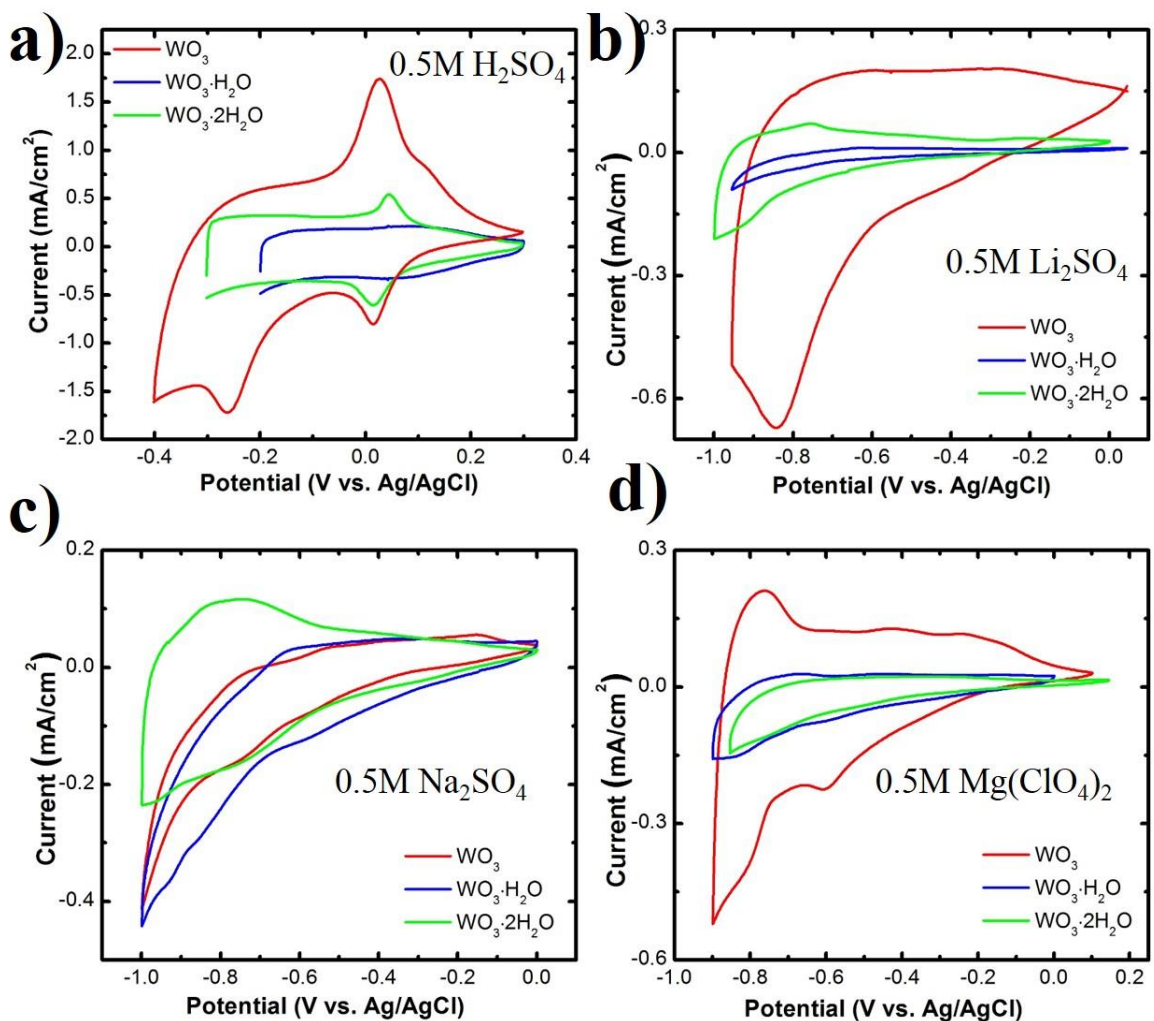


Figure 17. Cyclic voltammetry of the $\text{WO}_3 \cdot n\text{H}_2\text{O}$ materials at 2 mV/s in a) 0.5 M H_2SO_4 , b) 2 M Li_2SO_4 , c) 1 M Na_2SO_4 , and d) 0.5 M $\text{Mg}(\text{ClO}_4)_2$. Compared with the electrochemical behavior in acidic electrolyte, no significant charge storage occurs at neutral pH in the $\text{WO}_3 \cdot n\text{H}_2\text{O}$ materials as indicated by the low current density.

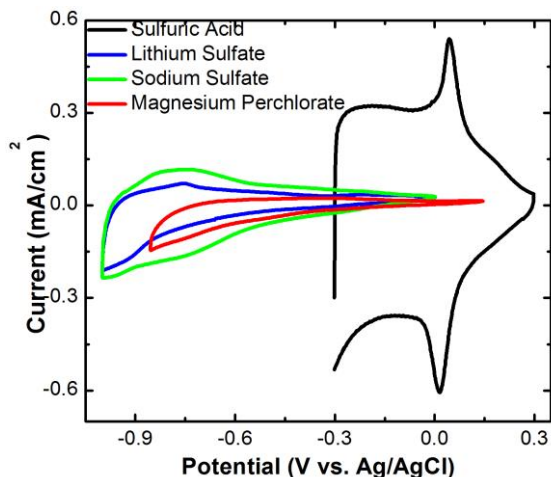


Figure 18. Cyclic voltammetry of $\text{WO}_3 \cdot 2\text{H}_2\text{O}$ in 0.5 M H_2SO_4 , 2 M Li_2SO_4 , 1 M Na_2SO_4 , and 0.5 M $\text{Mg}(\text{ClO}_4)_2$ at 2 mV/s. These results show that the electrochemical energy storage in the acidic electrolyte is significantly greater than in neutral pH electrolytes.

Figure 19 shows the cyclic voltammograms at various sweep rates from 2 – 200 mV/s for the $\text{WO}_3 \cdot n\text{H}_2\text{O}$ materials in 0.5 H_2SO_4 electrolyte. The background current from the carbon paper, acetylene black, and PVDF (“carbon background”) is also shown, and is negligible compared to the electrochemical response of the $\text{WO}_3 \cdot n\text{H}_2\text{O}$ materials. In these cyclic voltammetry experiments, the negative (cathodic) current corresponds to the intercalation of H^+ into the solid-state structure and the reduction of W^{6+} to W^{5+} . Upon sweep reversal to positive potentials, the positive (anodic) current corresponds to the oxidation of tungsten back to the +6 state, and the deintercalation of protons. The electrochemical potential window for each of the materials was limited by the onset potentials for the electrolysis of water, the

oxygen evolution reaction at high potentials and the hydrogen evolution reaction at low potentials, which occur at different potentials in the three $\text{WO}_3 \cdot n\text{H}_2\text{O}$ materials. The large current density from the electrolysis reactions would obscure the current due to energy storage. The evolution of oxygen also contributes to rusting of stainless steel components used in the three-electrode cell, which is another reason to avoid the reaction.

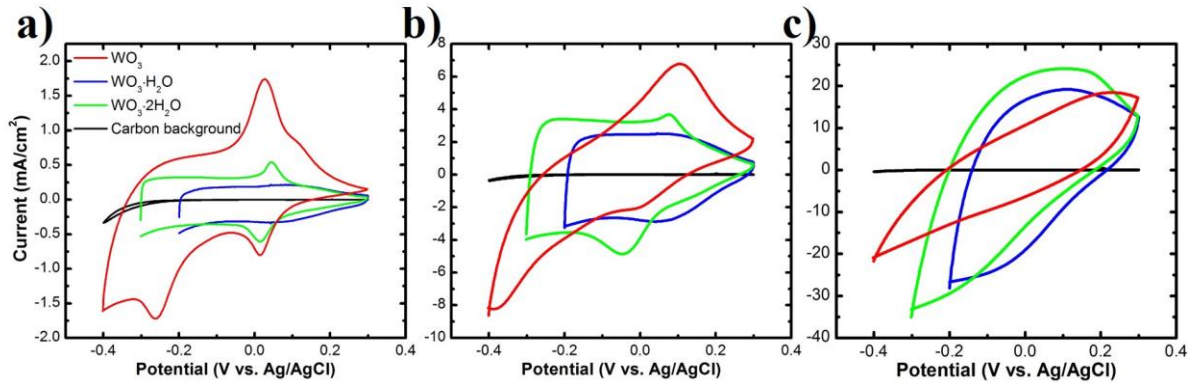


Figure 19. Cyclic voltammetry of the $\text{WO}_3 \cdot n\text{H}_2\text{O}$ materials in 0.5 M H_2SO_4 at a) 2 mV/s, b) 20 mV/s, and c) 200 mV/s. The background current from the carbon paper and acetylene black is included to show their negligible contribution.

Cyclic voltammetry at 2, 20, and 200 mV/s corresponds to charge/discharge times of 350-300 sec, 35-30 sec, and 3.5-3 sec, respectively, depending on the potential window for each of the $\text{WO}_3 \cdot n\text{H}_2\text{O}$ materials. These fast charge/discharge times were selected to investigate the power capability of the $\text{WO}_3 \cdot n\text{H}_2\text{O}$ materials (typical battery material charge/discharge times are on the order of hours). The charge storage capacity of a material is proportional to the area enclosed by the voltammogram. At 2 mV/s ($t = 350 - 300$ sec; **Figure 19a**) the capacity increases in the order $\text{WO}_3 > \text{WO}_3 \cdot 2\text{H}_2\text{O} > \text{WO}_3 \cdot \text{H}_2\text{O}$. However, at 200

mV/s ($t = 3.5 - 3$ sec; **Figure 19c**), the capacity increases in the order $\text{WO}_3 \cdot 2\text{H}_2\text{O} > \text{WO}_3 \cdot \text{H}_2\text{O} > \text{WO}_3$. Therefore, the presence of structural water appears to improve the high rate capability of a bulk, layered material.

The charge storage capacity of the $\text{WO}_3 \cdot n\text{H}_2\text{O}$ materials (**Figure 20**) calculated from the CVs at different sweep rates confirmed the conclusions from **Figure 19** that at high sweep rates, anhydrous WO_3 is worse than or equal to the capacity of the hydrated phases. The areal capacitance, C_A , from **Figure 20b** is calculated from the energy stored per cycle, E , by the following equation:

$$C_A = \frac{E}{AV} \quad (3.1)$$

where V is the potential window and A is the area of the electrode. The electrons stored per formula unit in **Figure 20c** is also calculated from E , but in electron volts, by the following equation:

$$\rho_e = \frac{mw * E[eV]}{m * N_A} \quad (3.2)$$

where mw is the molecular weight of the active material, m is the mass of the active material in the electrode, and N_A is Avogadro's number.

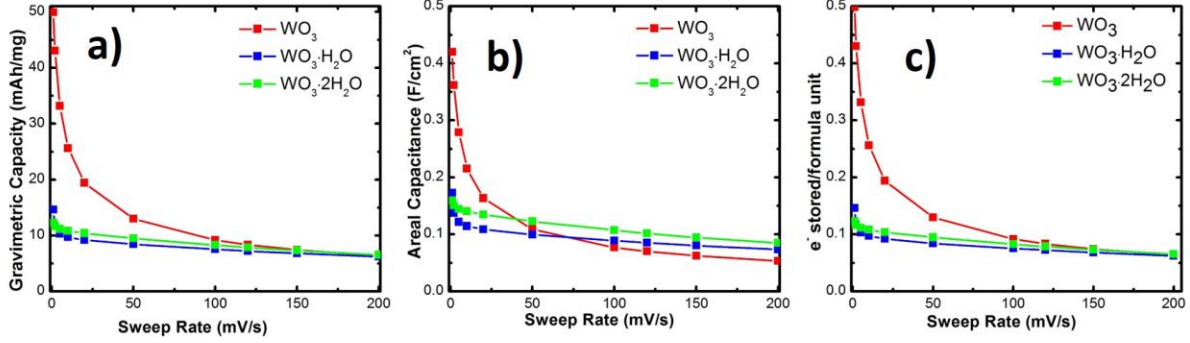


Figure 20. a) Gravimetric capacity, b) areal capacitance, and c) electrons stored per formula unit, for each of the $\text{WO}_3 \cdot n\text{H}_2\text{O}$ materials. The anhydrous WO_3 loses most of its capacity at 20 mV/s, while the capacity retention of the hydrated phases is much more stable even at high rates.

Kinetic analysis of the cyclic voltammograms was performed to determine whether the proton storage in the $\text{WO}_3 \cdot n\text{H}_2\text{O}$ materials is diffusion limited, as in most batteries, or surface controlled, as in EDLCs and pseudocapacitors. Generally, the current at a particular potential, $i(V)$, is dependent on the scan rate (ν) by the following equation:^{42–44}

$$i(\nu) = a\nu^b \quad (3.3)$$

where a and b are constants. The limiting values for b are $b = 0.5$, which corresponds to a process limited by semi-infinite linear diffusion, and $b = 1.0$, which corresponds to a surface controlled, or capacitive process. To determine the b -value, Equation 3.3 can be rearranged to:

$$\log(i(\nu)) = A + b \log(\nu) \quad (3.4)$$

where b is the slope of the line of $\log(i(\nu))$ vs. ν . This kinetic analysis was performed for both WO_3 and $\text{WO}_3 \cdot 2\text{H}_2\text{O}$, but not for $\text{WO}_3 \cdot \text{H}_2\text{O}$ because no definitive redox peak could be tracked as a function of the sweep rate. **Figure 21a** shows the cyclic voltammograms from 1 – 20 mV/s for WO_3 ; there are two different cathodic redox peaks present. These sweep rates were used

for the b -value analysis shown in **Figure 21b**. The b -values for the first peak (Peak 1, ~ 0 V vs. Ag/AgCl) and second peak (Peak 2, ~ -0.26 V vs. Ag/AgCl) in WO_3 are, respectively, 0.5 and 0.7. This is indicative of a mostly diffusion-controlled energy storage mechanism in WO_3 . **Figure 22a** and **b** show the cyclic voltammograms (from 1 – 50 mV/s) and b -value analysis for $\text{WO}_3 \cdot 2\text{H}_2\text{O}$. The dihydrate exhibits a single cathodic peak at ~ 0 V vs. Ag/AgCl with a b value of 0.90, which means that the energy storage mechanism is nearly completely surface controlled.

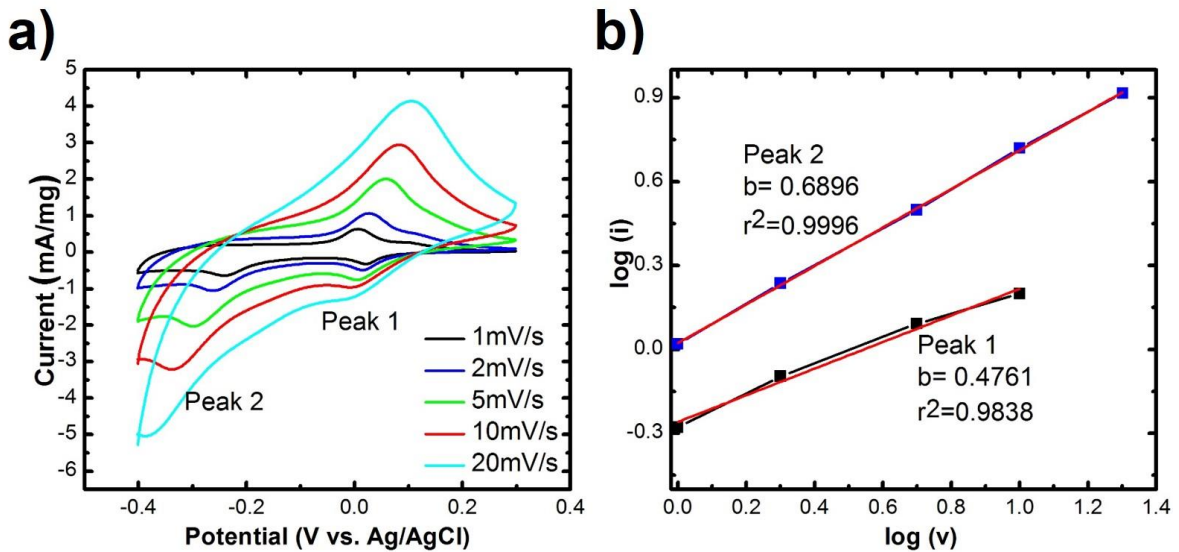


Figure 21. Kinetic analysis of the electrochemical energy storage behavior of WO_3 . a) Cyclic voltammetry from 1 – 20 mV/s and b) the b -value kinetic analysis for Peak 1 (~ 0 V vs. Ag/AgCl) and Peak 2 (~ -0.26 V vs. Ag/AgCl) using Equation 3.4. Since b is closer to 0.5 for both peaks, the energy storage is mainly diffusion controlled in WO_3 .

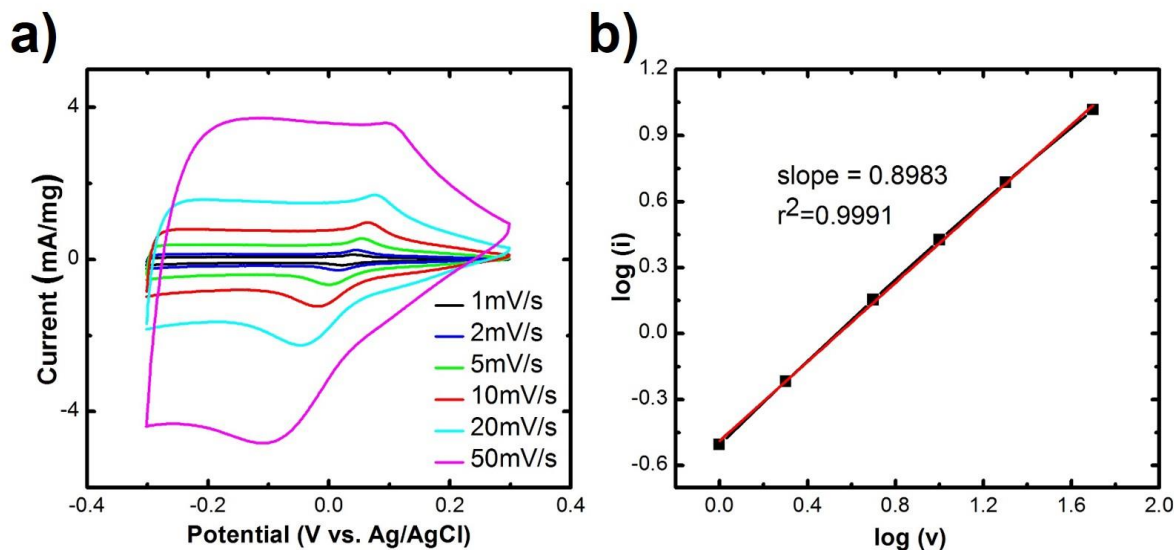


Figure 22. Kinetic analysis of the electrochemical energy storage behavior of $\text{WO}_3 \cdot 2\text{H}_2\text{O}$. a) Cyclic voltammetry from 1 – 50 mV/s and b) the b -value kinetic analysis for the cathodic peak at ~ 0 V vs. Ag/AgCl using Equation 3.4. Since b is closer to 1 for the peak, the process is mainly capacitive.

To determine the long-term stability of the $\text{WO}_3 \cdot n\text{H}_2\text{O}$ materials for EES, multiple cyclic voltammetry cycles were performed at different sweep rates. **Figure 23** shows the differences between the 2nd and 1000th cycle at 20 mV/s for the three $\text{WO}_3 \cdot n\text{H}_2\text{O}$ materials. The onset of the hydrogen evolution reaction shifts to more positive potentials after 1000 cycles for $\text{WO}_3 \cdot 2\text{H}_2\text{O}$ and WO_3 , and possibly $\text{WO}_3 \cdot \text{H}_2\text{O}$, although the onset potential is less obvious because its potential window ends at -0.2 V vs. Ag/AgCl. The shape of the cyclic voltammogram is least changed for the dihydrate, followed by the anhydrate and the

monohydrate. Overall, all three $\text{WO}_3 \cdot n\text{H}_2\text{O}$ materials exhibit fairly good cyclic stability at 20 mV/s.

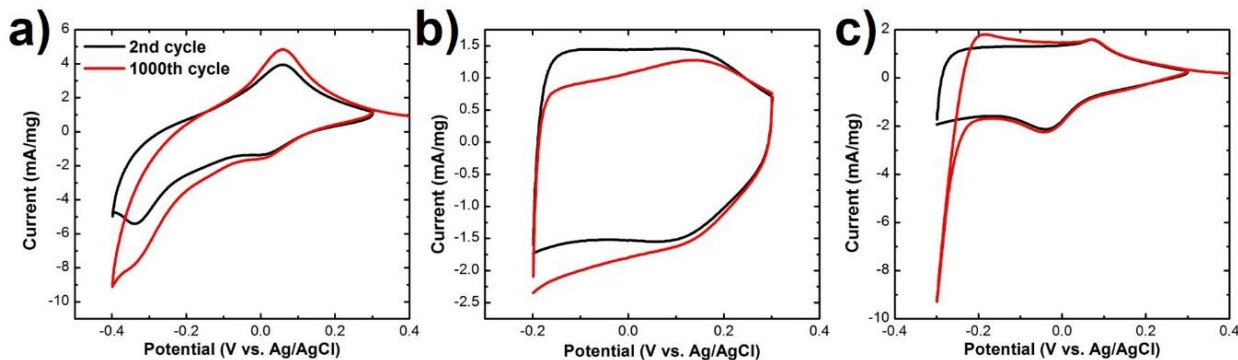


Figure 23. Cyclic voltammetry of the 2nd and 1000th cycle in 0.5 M H_2SO_4 at 20 mV/s for a) WO_3 , b) $\text{WO}_3 \cdot \text{H}_2\text{O}$, and c) $\text{WO}_3 \cdot 2\text{H}_2\text{O}$. Repeated cycling shifts the hydrogen evolution reaction to higher potentials. $\text{WO}_3 \cdot 2\text{H}_2\text{O}$ exhibits the best electrochemical stability as indicated by the similarity between the 2nd and 1000th cycles.

Figure 24 shows the % capacity retention as a function of cycle number at 20 and 200 mV/s for all three $\text{WO}_3 \cdot n\text{H}_2\text{O}$ materials in 0.5 M H_2SO_4 . The % capacity retention was calculated by taking the percentage of the measured charge stored to the maximum charged stored during all 1000 cycles. It is apparent that capacity retention is over 90% in all three $\text{WO}_3 \cdot n\text{H}_2\text{O}$ materials except for $\text{WO}_3 \cdot \text{H}_2\text{O}$ at 20 mV/s. In general, $\text{WO}_3 \cdot \text{H}_2\text{O}$ exhibits the lowest capacity retention at both 20 and 200 mV/s. For $\text{WO}_3 \cdot 2\text{H}_2\text{O}$, it appears that the material requires an “activation” period in order to achieve the best performance, as indicated by the increase in % capacity retention with cycle number. For WO_3 , the capacity retention decreases slowly with cycle number, suggesting that the structure deteriorates over time. This corresponds well with the cathodic peak kinetic analysis, where for WO_3 , the redox reaction is

mainly diffusion limited, and for $\text{WO}_3 \cdot 2\text{H}_2\text{O}$, the kinetics were mainly surface controlled, At 20 mV/s, the lower capacity retention of WO_3 could also be explained by the greater number of electrons stored by WO_3 , as indicated by **Figure 20c**.

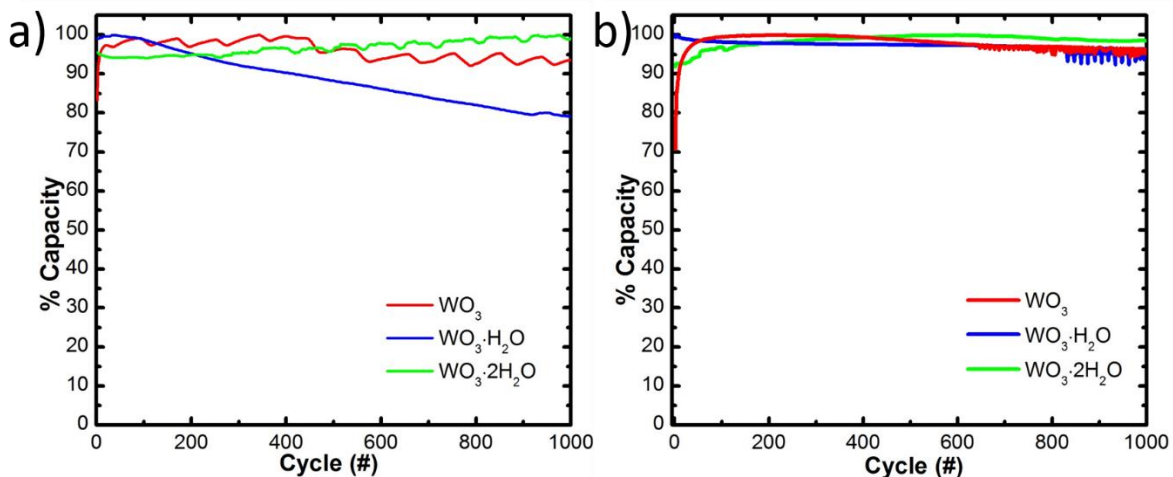


Figure 24. % capacity retention for the $\text{WO}_3 \cdot n\text{H}_2\text{O}$ materials at a) 20 mV/s and b) 200 mV/s in 0.5 M H_2SO_4 .

Self-discharge, or the tendency for an energy storage material to slowly lose charge over time, is a serious issue for high power energy storage. **Figure 25** shows the self-discharge of each of the $\text{WO}_3 \cdot n\text{H}_2\text{O}$ materials. The self-discharge measurements were performed by measuring the open-circuit potential (OCP) of each material every 15 minutes for 12 hours after driving the electrode down to the lowest negative potentials (as determined by the cyclic voltammetry potential windows) at a rate of 20 mV/s ($t = 350 - 300$ sec). From these curves, it can be seen that $\text{WO}_3 \cdot 2\text{H}_2\text{O}$ has the worst self-discharge, followed by $\text{WO}_3 \cdot \text{H}_2\text{O}$, and WO_3 .

It is possible that the structural water within $\text{WO}_3 \cdot 2\text{H}_2\text{O}$ and $\text{WO}_3 \cdot \text{H}_2\text{O}$, which is believed to facilitate the transport of protons through the material, can also lead to increased self-discharge.

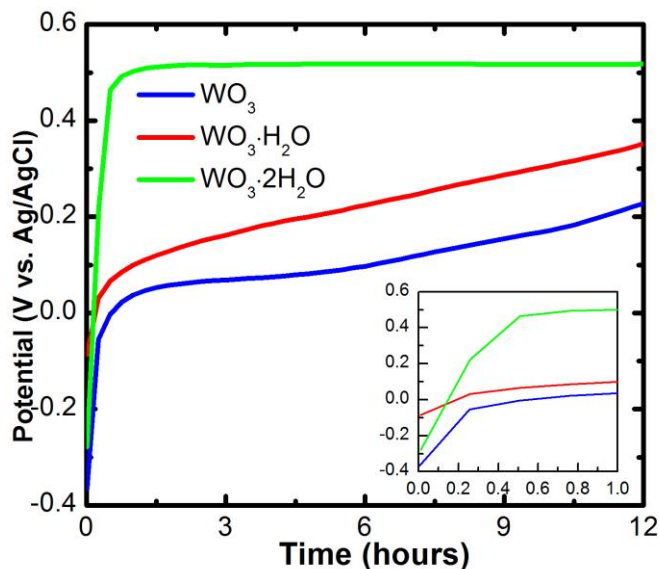


Figure 25. Self-discharge of the $\text{WO}_3 \cdot n\text{H}_2\text{O}$ materials over 12 hours, showing that the self-discharge rate increases as the amount of structural water increases.

3.4 *In-situ* and *Ex-situ* Characterization

In-situ Raman spectroscopy was used to study the local structure of the $\text{WO}_3 \cdot n\text{H}_2\text{O}$ materials during linear sweep voltammetry at 1 mV/s in 0.5 M H_2SO_4 (Figures 28-30). In order to obtain Raman spectra, linear sweep experiments were stopped at 100 mV intervals during the cathodic and anodic sweeps. The initial Raman spectra show the same peaks as dry, powdered samples. Furthermore, the cyclic voltammograms of $\text{WO}_3 \cdot n\text{H}_2\text{O}$ materials on screen printed electrodes (Figure 26) match those of the slurry-cast electrodes (Figure 19), although the reference potential shifts slightly and the potential windows are reduced in order to reduce

the noise from the hydrogen evolution reaction. As seen in **Figures 27a, 28a, and 29a**, the intensity of all of the Raman peaks is extinguished at potentials of -250 mV, -200 mV, and -250 mV (*vs.* Ag), respectively, for WO_3 , $\text{WO}_3 \cdot \text{H}_2\text{O}$, and $\text{WO}_3 \cdot 2\text{H}_2\text{O}$. These potentials correspond to the beginning of the proton intercalation and tungsten oxide reduction. It is likely that the intercalated protons and electrons are responsible for the change from semiconductive to metallic behavior, as expected for WO_3 bronzes.⁴⁵ Metallic, conductive materials are not Raman active because of the limited penetration of the laser light.⁴⁶ **Figures 27b, 28b, and 29b** show that the Raman peaks recover in intensity as the potentials become more positive. The recovery of the peaks corresponding to the various $\text{WO}_3 \cdot n\text{H}_2\text{O}$ phases is indicative that the structures were not destroyed during the intercalation/deintercalation process, and that semiconductive behavior has been restored upon proton deintercalation. However, even though the peaks recover, the magnitude of the intensity is lower, so it is likely that some amount of protons remain within the structures. This behavior corresponds well with previous

observations, where WO_3 was observed to be conductive at low cathodic potentials and not conductive at high anodic potentials in acidic solution.⁴⁷

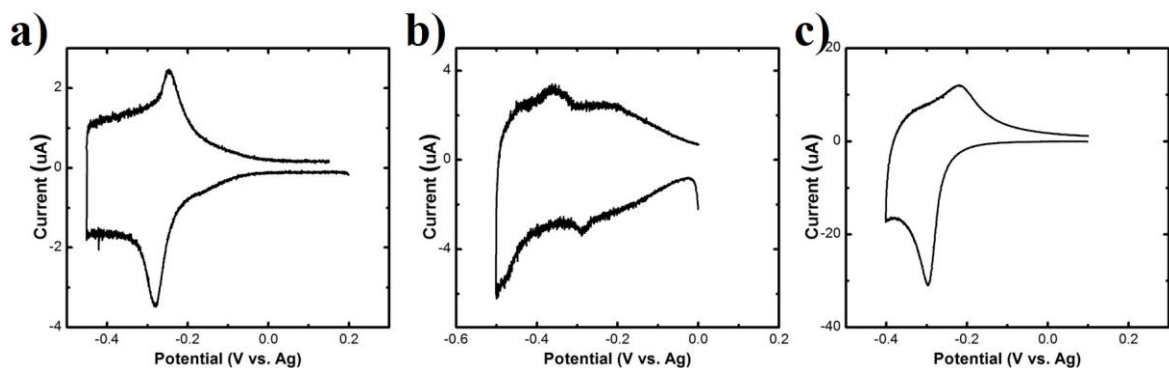


Figure 26. Cyclic voltammetry of the screen printed electrodes at 1 mV/s in 0.5 M H_2SO_4 for a) $\text{WO}_3 \cdot 2\text{H}_2\text{O}$ b) $\text{WO}_3 \cdot \text{H}_2\text{O}$ c) $\text{WO}_3 \cdot \text{H}_2\text{O}$ showing shifted CVs that match the slurry-cast electrodes in **Figure 19**.

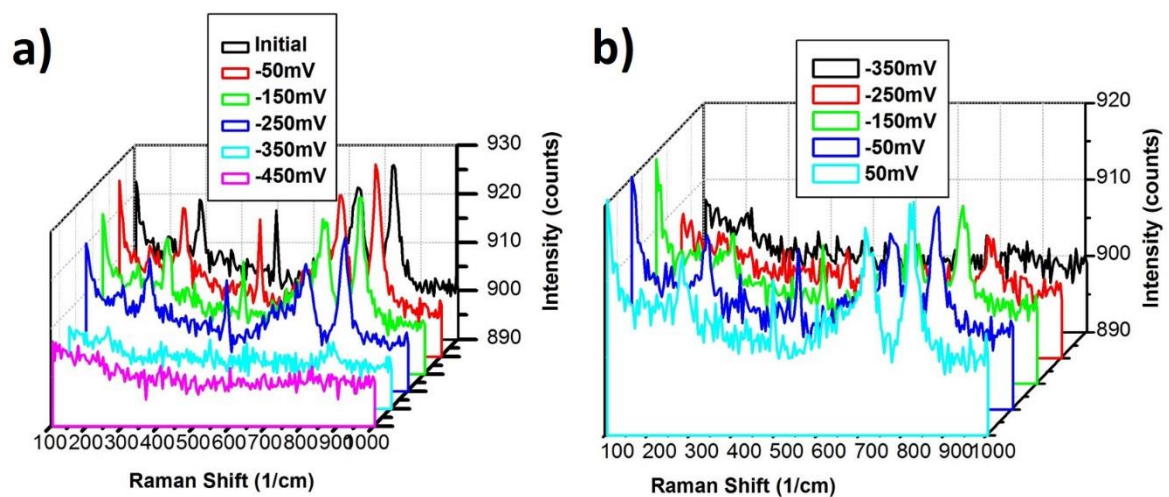


Figure 27. *In-situ* Raman measurements for WO_3 taken every 100 mV during a linear sweep voltammetry experiment in 0.5 M H_2SO_4 . a) Cathodic sweep from open circuit to -450 mV and b) Anodic sweep from -350 mV to 50mV.

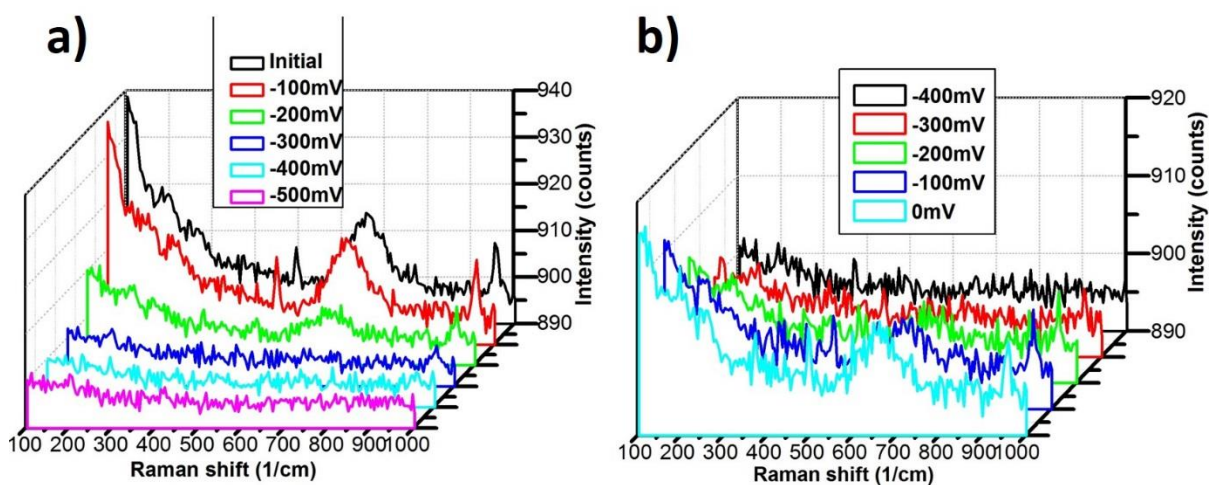


Figure 28. *In-situ* Raman measurements for $\text{WO}_3 \cdot \text{H}_2\text{O}$ taken every 100 mV during a linear sweep voltammetry experiment in 0.5 M H_2SO_4 . a) Cathodic sweep from open circuit to -500 mV and b) Anodic sweep from -400 mV to 0 mV.

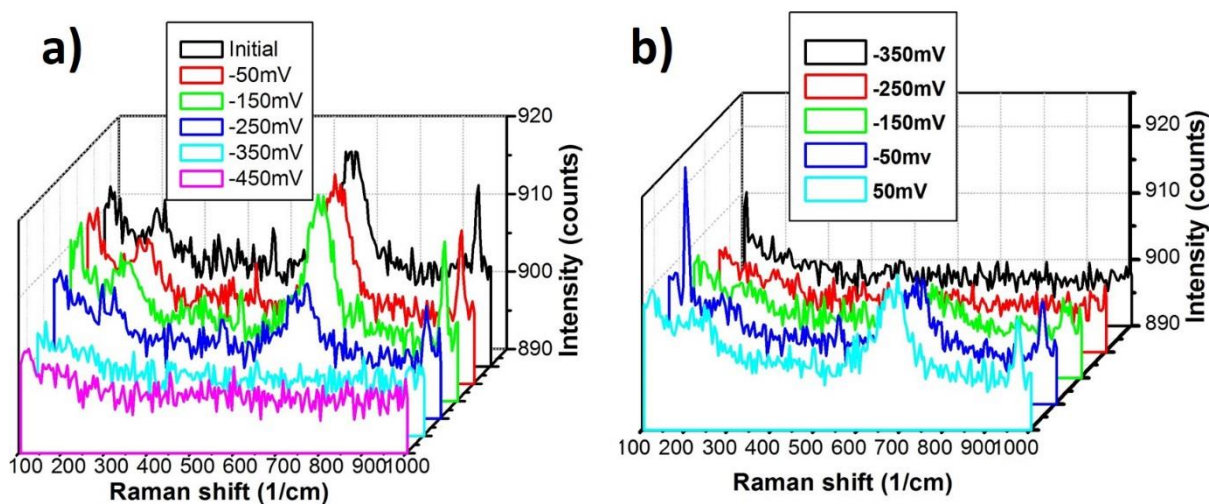


Figure 29. *In-situ* Raman measurements for $\text{WO}_3 \cdot 2\text{H}_2\text{O}$ taken every 100 mV during a linear sweep voltammetry experiment in 0.5 M H_2SO_4 . a) Cathodic sweep from open circuit to -450 mV and b) Anodic sweep from -350 mV to 50 mV.

Ex-situ XRD was performed on slurry-cast electrodes in order to determine the structure of the $\text{WO}_3 \cdot n\text{H}_2\text{O}$ after proton intercalation. **Figure 30** shows the XRD patterns of $\text{WO}_3 \cdot n\text{H}_2\text{O}$ before and after a linear sweep experiment at 1mV/s to negative potentials, as indicated in the inset. Carbon paper exhibits a strong peak at $\sim 26^\circ$, which obscures some of the diffraction peaks of the active materials. However, the different hydration states can still easily be differentiated based on the distinctive peaks at $\sim 12^\circ$ for $\text{WO}_3 \cdot 2\text{H}_2\text{O}$ and 16° for $\text{WO}_3 \cdot \text{H}_2\text{O}$. For all three materials, it appears that the structure is preserved after the sweep to the negative potential. Because there is no phase change upon cycling to the negative potential nor is there an appreciable increase in the interlayer spacing, it makes sense that the capacity of each of the materials remains reasonably high after 1000 cycles.

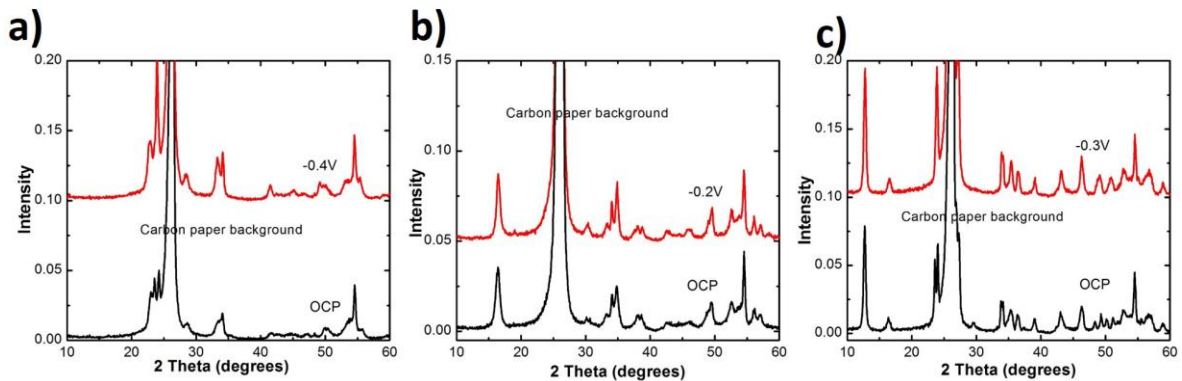


Figure 30. *Ex-situ* XRD of $\text{WO}_3 \cdot n\text{H}_2\text{O}$ at open circuit potential and various cathodic potentials (as indicated in the inset, vs. Ag/AgCl) in 0.5 M H_2SO_4 : a) WO_3 , b) $\text{WO}_3 \cdot \text{H}_2\text{O}$, and c) $\text{WO}_3 \cdot 2\text{H}_2\text{O}$. All three materials store protons via a solid solution intercalation reaction, since there are no new phases.

Chapter 4 – Conclusions and Future Work

4.1 Conclusions

The motivation for this thesis was that the presence of structural water could lead to improved rate capability in bulk, layered materials for EES. This research investigated the electrochemical behavior of model, redox-active hydrated transition metal oxides, $\text{WO}_3 \cdot 2\text{H}_2\text{O}$ and $\text{WO}_3 \cdot \text{H}_2\text{O}$, and compared their behavior with anhydrous WO_3 for high rate electrochemical energy storage. Physical characterization, cyclic voltammetry in various electrolytes, *in-situ* Raman spectroscopy, and *ex-situ* XRD were performed in order to relate the electrochemical behavior with the material structure. In summary, the thesis found the following main conclusions:

- 1) The $\text{WO}_3 \cdot n\text{H}_2\text{O}$ are not electrochemically active in neutral pH aqueous electrolytes; an acidic electrolyte is necessary to observe significant energy storage.
- 2) $\text{WO}_3 \cdot 2\text{H}_2\text{O}$ exhibits superior capacity retention at fast sweep rates as compared with WO_3 . This is attributed to the presence of structural water for fast proton transport.
- 3) Kinetic analysis of the cyclic voltammograms shows that diffusion-controlled currents are associated with the redox reaction in WO_3 , while capacitive currents are associated with the redox in $\text{WO}_3 \cdot 2\text{H}_2\text{O}$.
- 4) There are no phase changes observed by Raman spectroscopy or XRD during electrochemical cycling of $\text{WO}_3 \cdot 2\text{H}_2\text{O}$, $\text{WO}_3 \cdot \text{H}_2\text{O}$, or WO_3 .
- 5) All $\text{WO}_3 \cdot n\text{H}_2\text{O}$ undergo a semiconductor-to-metal transition upon electrochemical proton intercalation, as evidenced by the complete extinction of the Raman spectra at negative potentials.

- 6) $\text{WO}_3 \cdot \text{H}_2\text{O}$ exhibits poor cyclability and capacity as compared with $\text{WO}_3 \cdot 2\text{H}_2\text{O}$ and WO_3 , which may be due to the destabilization of the structure from corner-sharing octahedrons in the WO_3 and without the stabilization of the interlayer water molecules of $\text{WO}_3 \cdot 2\text{H}_2\text{O}$.

4.2 Future Work

- 1) The effect of other structural molecules on the kinetics of charge storage reaction can be investigated by using solvent exchange methods. It is possible that other molecules could produce superior properties. By extension, exchanging the solvent with a larger molecule would eventually lead to exfoliation of the layered structures into nanosheets, which may also produce different electrochemical behavior than the bulk oxide.
- 2) Investigation into the effects of electrode structure on charge storage properties should be conducted. The slurry electrodes used in this thesis were of varying textures and thicknesses, even though efforts were put into making the electrodes as homogenous as possible. Preliminary results using a rolling mill to flatten electrodes showed a degradation in the charge storage properties, which is not expected since electrode pressing usually improves the electronic contact between the active material and the current collector. Furthermore, impedance measurements produced varying results which are attributed to the differences in electrode fabrication.
- 3) Creating a solid solution of WO_3 hydrates with other materials such as MoO_3 may improve the EES behavior. For example, a mixture of WO_3 and MoO_3 may stabilize MoO_3 in aqueous electrolytes while increasing the gravimetric capacity of the electrode by reducing the amount of heavy tungsten.

- 4) Determine the reason why $\text{WO}_3 \cdot n\text{H}_2\text{O}$ do not store cations in neutral pH electrolytes. For large-scale grid storage applications, it is of great interest to perform energy storage in low-cost, aqueous, and neutral pH electrolytes.

REFERENCES

1. Cronshaw, I. World Energy Outlook 2014 projections to 2040: natural gas and coal trade, and the role of China. *Aust. J. Agric. Resour. Econ.* **59**, 571–585 (2015).
2. Annual Energy Outlook 2014 - Energy Information Administration. Available at: <http://www.eia.gov/forecasts/archive/aeo14/>. (Accessed: 27th July 2016)
3. Rastler, D. Electric Energy Storage Technology Options: A White Paper Primer on Applications, Costs, and Benefits. (2010).
4. Bagher, A. M., Vahid, M., Mohsen, M. & Parvin, D. Hydroelectric Energy Advantages and Disadvantages. *Am. J. Energy Sci.* **2**, 17 (2015).
5. Zhang, L. L. & Zhao, X. S. Carbon-based materials as supercapacitor electrodes. *Chem. Soc. Rev.* **38**, 2520–2531 (2009).
6. Fukuhara, M., Kuroda, T. & Hasegawa, F. Realizing a supercapacitor in an electrical circuit. *Appl. Phys. Lett.* **105**, 202904 (2014).
7. Sharma, S. & Ghoshal, S. K. Hydrogen the future transportation fuel: From production to applications. *Renew. Sustain. Energy Rev.* **43**, 1151–1158 (2015).
8. Ball, M. & Weeda, M. The hydrogen economy – Vision or reality?1. *Int. J. Hydrog. Energy* **40**, 7903–7919 (2015).
9. Coyle, W. T. USDA Economic Research Service - The Future of Biofuels: A Global Perspective. Available at: <http://www.ers.usda.gov/amber-waves/2007-november/the-future-of-biofuels-a-global-perspective.aspx#.V5gUYfkrKUK>. (Accessed: 27th July 2016)
10. Rolison, D. R. *et al.* Multifunctional 3D nanoarchitectures for energy storage and conversion. *Chem. Soc. Rev.* **38**, 226–252 (2008).

11. Conway, B. E. *Electrochemical supercapacitors : scientific fundamentals and technological applications*. (Plenum Press, c1999.).
12. Jayalakshmi, M. & Balasubramanian, K. Simple Capacitors to Supercapacitors-An Overview. *ResearchGate* **3**, 1196–1217 (2008).
13. Zhou, X. *et al.* A renewable bamboo carbon/polyaniline composite for a high-performance supercapacitor electrode material. *J. Solid State Electrochem.* **16**, 877–882 (2011).
14. Kalpana, D. *et al.* Recycled waste paper—A new source of raw material for electric double-layer capacitors. *J. Power Sources* **190**, 587–591 (2009).
15. Kang, B. & Ceder, G. Battery materials for ultrafast charging and discharging. *Nature* **458**, 190–193 (2009).
16. Simon, P. & Gogotsi, Y. Materials for electrochemical capacitors. *Nat. Mater.* **7**, 845–854 (2008).
17. Miller, J. R. Electrochemical Capacitors: Challenges and Opportunities for Real-World Applications. Available at: https://www.electrochem.org/dl/interface/spr/spr08/spr08_p53-57.pdf. (Accessed: 31st May 2016)
18. Augustyn, V., Simon, P. & Dunn, B. Pseudocapacitive oxide materials for high-rate electrochemical energy storage. *Energy Environ. Sci.* **7**, 1597–1614 (2014).
19. Lee, H. Y. & Goodenough, J. B. Supercapacitor Behavior with KCl Electrolyte. *J. Solid State Chem.* **144**, 220–223 (1999).

20. Trasatti, S. & Buzzanca, G. Ruthenium dioxide: A new interesting electrode material. Solid state structure and electrochemical behaviour. *J. Electroanal. Chem. Interfacial Electrochem.* **29**, A1–A5 (1971).
21. Zheng, J. P., Cygan, P. J. & Jow, T. R. Hydrrous Ruthenium Oxide as an Electrode Material for Electrochemical Capacitors. *J. Electrochem. Soc.* **142**, 2699–2703 (1995).
22. Kumagai, N., Kumagai, N. & Tanno, K. Electrochemical characteristics and structural changes of molybdenum trioxide hydrates as cathode materials for lithium batteries. *J. Appl. Electrochem.* **18**, 857–862 (1988).
23. Ayyappan, S. & Rangavittal, N. A thermal dehydration study of $\text{WO}_3 \cdot 2\text{H}_2\text{O}$. *Bull. Mater. Sci.* **20**, 103–109 (1997).
24. Khyzhun, O. Y. & Solonin, Y. M. Electronic structure of the monoclinic and hexagonal trioxides of tungsten and hexagonal hydrogen tungsten bronze $\text{H}_0.24\text{WO}_3$. *Powder Metall. Met. Ceram.* **39**, 287–294 (2000).
25. Hurditch, R. Electrochromism in hydrated tungsten-oxide films. *Electron. Lett.* **11**, 142 (1975).
26. Svensson, J. S. E. M. & Granqvist, C. G. Electrochromic tungsten oxide films for energy efficient windows. *Sol. Energy Mater.* **11**, 29–34 (1984).
27. Bechinger, C., Oefinger, G., Herminghaus, S. & Leiderer, P. On the fundamental role of oxygen for the photochromic effect of WO_3 . *J. Appl. Phys.* **74**, 4527–4533 (1993).
28. Hersh, H. N., Kramer, W. E. & McGee, J. H. Mechanism of electrochromism in WO_3 . *Appl. Phys. Lett.* **27**, 646–648 (1975).

29. McIntyre, J. D. E., Basu, S., Peck, W. F., Brown, W. L. & Augustyniak, W. M. Cation insertion reactions of electrochromic tungsten and iridium oxide films. *Phys. Rev. B* **25**, 7242–7254 (1982).
30. Díaz-Reyes, J., Dorantes-García, V., Pérez-Benítez, A. & Balderas-López, J. A. Obtaining of films of tungsten trioxide (WO₃) by resistive heating of a tungsten filament. *Superf. Vacío* **21**, 12–17 (2008).
31. de Grothuss, C. J. T. Memoir on the decomposition of water and of the bodies that it holds in solution by means of galvanic electricity. *Biochim. Biophys. Acta BBA - Bioenerg.* **1757**, 871–875 (2006).
32. Swanson, J. M. J. *et al.* Proton Solvation and Transport in Aqueous and Biomolecular Systems: Insights from Computer Simulations. *J. Phys. Chem. B* **111**, 4300–4314 (2007).
33. England, W. A., Cross, M. G., Hamnett, A., Wiseman, P. J. & Goodenough, J. B. Fast proton conduction in inorganic ion-exchange compounds. *Solid State Ion.* **1**, 231–249 (1980).
34. Sugimoto, W., Yokoshima, K., Murakami, Y. & Takasu, Y. Charge storage mechanism of nanostructured anhydrous and hydrous ruthenium-based oxides. *Electrochimica Acta* **52**, 1742–1748 (2006).
35. Gao, W. *et al.* Direct laser writing of micro-supercapacitors on hydrated graphite oxide films. *Nat. Nanotechnol.* **6**, 496–500 (2011).
36. Li, Y. M., Hibino, M., Miyayania, M. & Kudo, T. Proton conductivity of tungsten trioxide hydrates at intermediate temperature. *Solid State Ion.* **134**, 271–279 (2000).

37. Lin, H. Density Functional Theory Investigation of Proton Diffusion in Tungsten Oxide And Its Hydrates. *eScholarship* (2014).
38. Freedman, M. L. The Tungstic Acids. *J. Am. Chem. Soc.* **81**, 3834–3839 (1959).
39. Dieing, T., Hollricher, O. & Toporski, J. *Confocal Raman microscopy [electronic resource]*. (Springer, c2010.).
40. Bard, A. J. & Faulkner, L. R. *Electrochemical methods : fundamentals and applications*. (Wiley, c2001.).
41. Daniel, M. F., Desbat, B., Lassegues, J. C., Gerand, B. & Figlarz, M. Infrared and Raman study of WO₃ tungsten trioxides and WO₃·xH₂O tungsten trioxide hydrates. *J. Solid State Chem.* **67**, 235–247 (1987).
42. Wang, J., Polleux, J., Lim, J. & Dunn, B. Pseudocapacitive Contributions to Electrochemical Energy Storage in TiO₂ (Anatase) Nanoparticles. *J. Phys. Chem. C* **111**, 14925–14931 (2007).
43. Liu, T.-C., Pell, W. G., Conway, B. E. & Roberson, S. L. Behavior of Molybdenum Nitrides as Materials for Electrochemical Capacitors Comparison with Ruthenium Oxide. *J. Electrochem. Soc.* **145**, 1882–1888 (1998).
44. Brezesinski, K. *et al.* Pseudocapacitive Contributions to Charge Storage in Highly Ordered Mesoporous Group V Transition Metal Oxides with Iso-Oriented Layered Nanocrystalline Domains. *J. Am. Chem. Soc.* **132**, 6982–6990 (2010).
45. Liang, L. *et al.* High-performance flexible electrochromic device based on facile semiconductor-to-metal transition realized by WO₃·2H₂O ultrathin nanosheets. *Sci. Rep.* **3**, (2013).
46. Szymanski, H. A. *Raman spectroscopy: theory and practice*,. (Plenum Press, 1967).

47. Shen, P. K., Huang, H. T. & Tseung, A. C. C. A Study of Tungsten Trioxide and Polyaniline Composite Films I. Electrochemical and Electrochromic Behavior. *J. Electrochem. Soc.* **139**, 1840–1845 (1992).